

CAP4D: Creating Animatable 4D Portrait Avatars with Morphable Multi-View Diffusion Models

Felix Taubner^{1,2}

Ruihang Zhang¹

Mathieu Tuli³

David B. Lindell^{1,2}

¹University of Toronto ²Vector Institute ³LG Electronics

<https://felixtaubner.github.io/cap4d>

Abstract

Reconstructing photorealistic and dynamic portrait avatars from images is essential to many applications including advertising, visual effects, and virtual reality. Depending on the application, avatar reconstruction involves different capture setups and constraints—for example, visual effects studios use camera arrays to capture hundreds of reference images, while content creators may seek to animate a single portrait image downloaded from the internet. As such, there is a large and heterogeneous ecosystem of methods for avatar reconstruction. Techniques based on multi-view stereo or neural rendering achieve the highest quality results, but require hundreds of reference images. Recent generative models produce convincing avatars from a single reference image, but visual fidelity yet lags behind multi-view techniques. Here, we present CAP4D: an approach that uses a morphable multi-view diffusion model to reconstruct photoreal 4D (dynamic 3D) portrait avatars from any number of reference images (i.e., one to 100) and animate and render them in real time. Our approach demonstrates state-of-the-art performance for single-, few-, and multi-image 4D portrait avatar reconstruction, and takes steps to bridge the gap in visual fidelity between single-image and multi-view reconstruction techniques.

1. Introduction

Reconstructing realistic human avatars from images is a sought-after capability for applications including advertising, cinema, content creation, teleconferencing, and virtual reality. Depending on the application, avatar reconstruction involves different capture setups and constraints—from elaborate visual effects workflows involving hundreds of reference images [2] to more constrained settings where content creators seek to animate a single “in-the-wild” image [79]. In every application, photorealism and fidelity to the subject’s likeness are paramount. In this paper, we seek a general method to reconstruct photorealistic 4D (dynamic 3D) portrait avatars that are consistent with the likeness of any number of input reference images—e.g., from one to

100—while enabling real-time animation and rendering.

Conventional methods for reconstructing photorealistic, animatable avatars rely on setups involving camera arrays [2, 50, 53, 58] or monocular video sequences [30, 32, 44, 91, 115]. These setups aim to capture sufficient variation in poses and expressions to enable 4D avatar reconstruction, often through multi-view stereo [29] or neural rendering techniques [84]. However, these methods struggle to produce accurate results if the captured reference images lack sufficient diversity in poses or expressions.

To address this limitation, recent techniques leverage large datasets of 2D portrait images [45, 65, 92] and 3D scans [20, 33, 99, 116] to train diffusion models that capture robust priors on human appearance, enabling the reconstruction of 2D [85], 3D [36, 68], or 4D avatars [18] from a single reference image. Still, most diffusion-based methods focus on 2D representations [17, 24, 36, 85, 93], and inference with diffusion models is computationally expensive, which is a major obstacle to real-time rendering and animation. Moreover, no existing technique for 4D avatar reconstruction scales seamlessly from one to hundreds of reference images while consistently providing photorealistic results.

Here, we introduce CAP4D, a method that uses a morphable multi-view diffusion model (MMDM) to reconstruct photoreal 4D avatars that are based on any number of reference images and that are animated and rendered in real time (see Figure 1). Similar to other multi-view diffusion models [18, 31, 57, 78], MMDMs generate novel views of a scene based on reference images and pose conditioning. Our approach uses a 3D morphable model (3DMM) [9, 53] to provide pose and expression conditioning for the reference images [83] and to control the appearance of the generated images.

CAP4D reconstructs 4D avatars in two stages. In the first stage, the MMDM uses an iterated generation process to synthesize hundreds of images from novel viewpoints with a wide range of expressions. While the MMDM nominally supports only a limited number of reference and generated images, we lift this restriction through a stochastic input/output (I/O) conditioning procedure inspired by re-

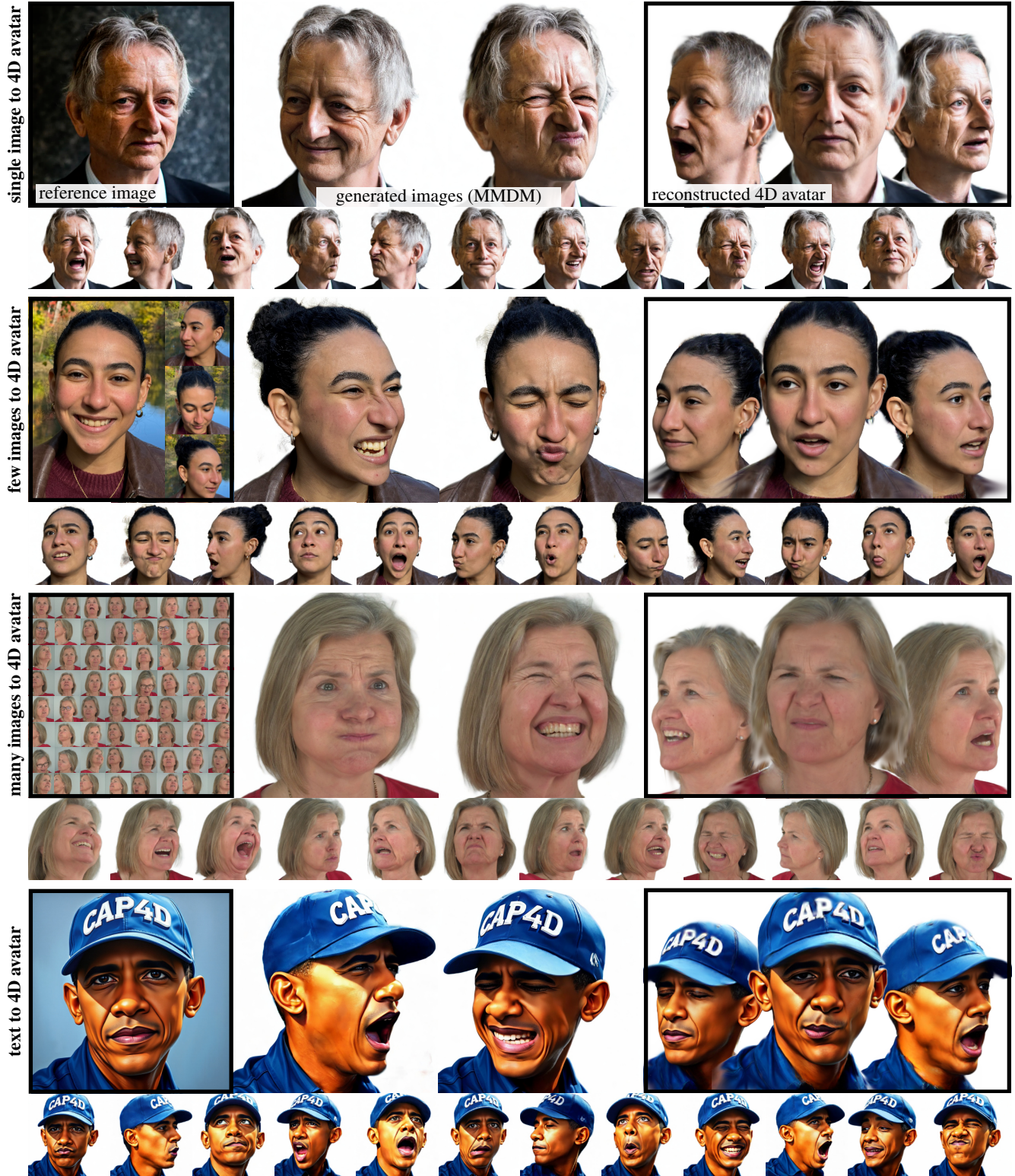


Figure 1. We present CAP4D: a method that generates 4D portrait avatars based on an arbitrary number of reference images (e.g., from one to one hundred) and animates them in real time. Our approach uses a morphable multi-view diffusion model to predict novel views with unseen expressions. For each subject, we generate hundreds of such views and train an animatable avatar using a representation based on 3D Gaussian splatting. Our method demonstrates state-of-the-art results for portrait view synthesis from a single image, monocular videos, or multi-view camera setups based on visual quality, identity consistency, 3D structure, and temporal consistency.

cent work on view synthesis [90] and video generation [52]. Specifically, at different steps of the reverse diffusion process [80], we condition the diffusion model on different input reference images and noisy generated outputs, enabling generation of hundreds of novel views based on a large number of reference images. In the second stage, we use the generated images to train a real-time 4D avatar based on 3D Gaussian splatting [69]. We augment the representation with an expression dependent appearance model to improve photorealism, and the resulting avatar can be animated and rendered in real time. Our approach outperforms other methods for view synthesis and animation of head avatars that use one, few, or many reference images as input, and is thus relevant to a broad range of applications.

Overall we make the following contributions.

- We introduce an MMDM for multi-view portrait image generation with pose and expression control, and we propose a stochastic I/O conditioning procedure to generate self-consistent portrait images given an arbitrary number of input reference images and novel viewpoints.
- We develop a technique to distill generated portrait images into a 4D avatar that is animated and rendered in real time.
- We perform an extensive evaluation of our approach for self-reenactment and cross-identity reenactment from one or more reference images, and we demonstrate state-of-the-art results for these tasks.

2. Related Work

Our work is connected to methods for avatar reconstruction that use different types of input data (e.g., multi-view imagery, monocular video, or single images).

Monocular and multi-view avatar reconstruction. Previous work reconstructs animatable 3D avatars from multi-view images or monocular video using textured mesh models [4, 15, 35, 44, 60, 111], volumetric representations [7, 34, 115], or point-based representations [112]. Textured mesh models are efficient to render and can be animated using 3DMMs [9]; however, they often fail to represent detailed structures like hair or teeth. Alternatively, volumetric representations model fine-grained appearance and produce photoreal results, but they are more computationally expensive to render [64]. Further, they require more sophisticated dynamics models, such as conditioning on 3DMM parameters [3, 30, 110] or learned latent codes [34]. While point-based methods can be animated via deformation [112], they face a tradeoff between rendering efficiency and photorealism based on the number of points in the representation. CAP4D builds on 3D Gaussian splatting [47]—a hybrid between point-based and volumetric representations that represents scenes using Gaussian primitives, is efficient to optimize, and achieves photoreal reconstruction

quality [43, 76, 91, 97]. We adapt a real-time representation based on GaussianAvatars [69], which we optimize based on the output of the MMDM.

Single image avatar reconstruction. By leveraging priors learned from large datasets, single-image methods directly regress 3D avatar representations based on textured meshes [48, 99, 116], feature grids [22, 49, 54, 61, 86, 87], or neural radiance fields [70, 114]. They perform novel view synthesis with expression control via 3DMMs, conditioning with latent codes, or predicted deformation fields [19, 26, 89, 96, 98, 100, 102]. Other approaches operate entirely in 2D, and render novel expressions and poses through learned warping and inpainting operations applied to a reference image [14, 25, 37, 71, 79, 95, 101, 103–105]. Overall, techniques for directly regressing 3D representations require prediction in a canonical space, which can fail with extreme head poses or strong variations in appearance (e.g., non-photoreal or animated scenes). 2D techniques often fail to inpaint discluded regions when head pose deviates significantly from the reference image. CAP4D sidesteps the limitations of these methods by using the MMDM to generate multi-view images based on one or more reference images; then we use iterative optimization to reconstruct the 4D avatar. Thus, our approach inherits the strengths of learned priors and iterative reconstruction methods.

Multi-view diffusion models. Our work builds on rapid progress in the areas of 2D and 3D generation [12, 27, 41, 77]. We leverage latent diffusion models [72], which were developed for image and video generation [8, 11, 16, 38] and enable synthesis of 3D or 4D objects [5, 6, 67, 81] and 3D or 4D avatars [68, 106, 113]. We also build on multi-view diffusion models [78] that generate multiple images of the same scene simultaneously for 3D reconstruction. In this vein, we are inspired by CAT3D [31], which trains a multi-view diffusion model on large image datasets; at inference time, hundreds of novel views are generated from a single image to reconstruct the scene in 3D. Our approach uses a similar generate-and-reconstruct paradigm, but we generate dynamic avatars rather than static scenes, and we enable controllable real-time rendering. Close to our work, Chen et al. [18] train a morphable multi-view diffusion model conditioned on 3DMM information for single-image 3D avatar reconstruction. Given a reference image, they generate a fixed number of novel views with controllable expressions and then directly infer a 3D representation. However, their approach cannot generate consistent video frames and does not support real-time rendering.

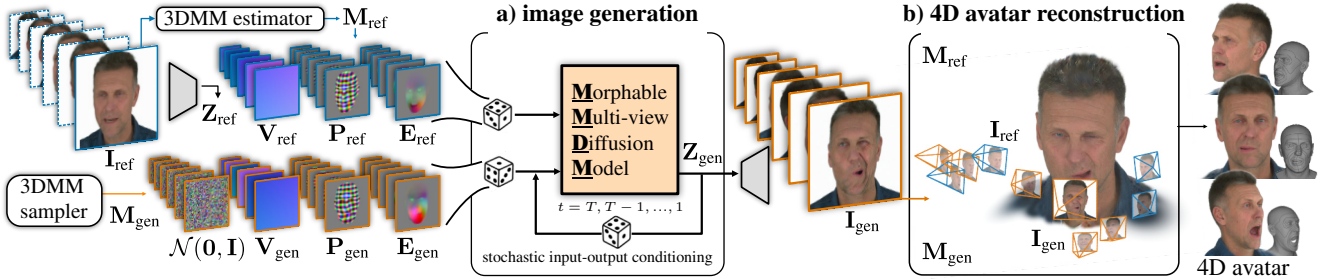


Figure 2. Overview of CAP4D. (a) The method takes as input an arbitrary number of reference images \mathbf{I}_{ref} that are encoded into the latent space of a variational autoencoder [72]. An off-the-shelf face tracker estimates a 3DMM, \mathbf{M}_{ref} , for each reference image, from which we derive conditioning signals that describe camera view direction, \mathbf{V}_{ref} , head pose \mathbf{P}_{ref} , and expression \mathbf{E}_{ref} . We associate additional conditioning signals with each input noisy latent image based on the desired generated viewpoints, poses, and expressions. The MMDM generates images through a stochastic input–output conditioning procedure that randomly samples reference images and generated images during each step of the iterative image generation process. (b) The generated and reference images are used with the tracked and sampled 3DMMs to reconstruct a 4D avatar based on a 3D Gaussian splatting representation [47, 69].

3. Method

CAP4D consists of two main stages: (1) a morphable multi-view diffusion model that generates a large number of novel views from input reference images, and (2) an animatable 4D representation based on 3D Gaussian splatting representation that is reconstructed from the reference and generated images. We provide an overview of CAP4D in Figure 2.

3.1. Morphable Multi-View Diffusion Model

We train an MMDM that takes a set of R reference images, $\mathbf{I}_{\text{ref}} = \{\mathbf{i}_{\text{ref}}^{(r)}\}_{r=1}^R$, as input and outputs G generated images, $\mathbf{I}_{\text{gen}} = \{\mathbf{i}_{\text{gen}}^{(g)}\}_{g=1}^G$. The model is conditioned on additional information including the head pose, expression, and camera view direction for each reference and generated image, given as $\mathbf{C}_{\text{ref}} = \{\mathbf{c}_{\text{ref}}^{(r)}\}_{r=1}^R$ and $\mathbf{C}_{\text{gen}} = \{\mathbf{c}_{\text{gen}}^{(g)}\}_{g=1}^G$. In this way, the MMDM learns the joint probability of generated images:

$$P(\mathbf{I}_{\text{gen}} | \mathbf{I}_{\text{ref}}, \mathbf{C}_{\text{ref}}, \mathbf{C}_{\text{gen}}). \quad (1)$$

Architecture. Our model is initialized from Stable Diffusion 2.1 [72], and we adapt the architecture for multi-view generation following previous work [31]. Specifically, we use a pre-trained image auto-encoder [72] to encode images into a low-resolution latent space, and we use the latent diffusion model to process R reference latent images, \mathbf{Z}_{ref} , and G generated latent images \mathbf{Z}_{gen} in parallel. To share information between the processed latents for each image, we replace 2D attention layers after 2D residual blocks with 3D attention (i.e., two spatial dimensions and one dimension across input images). We also remove the cross-attention layers since we do not use a text conditioning input. We fine-tune the model by optimizing all parameters.

The model is conditioned on additional images that provide the head pose, expression, camera view and other con-

textual information for each reference and generated image. These conditioning images consist of (1) *3D pose maps*, $\mathbf{P}_{\text{ref/gen}}$, that provide the rasterized canonical 3D coordinates of the head geometry; (2) *expression deformation maps*, $\mathbf{E}_{\text{ref/gen}}$, containing the rasterized 3D deformations of the geometry relative to the neutral expression mesh; (3) *view direction maps*, $\mathbf{V}_{\text{ref/gen}}$, showing the direction of each camera ray in the first camera reference frame; and (4) binary masks $\mathbf{B}_{\text{ref/gen}}$ that indicate whether the input is a reference or generated image. We express the conditioning information for the reference images as $\mathbf{C}_{\text{ref}} = \{\mathbf{P}_{\text{ref}}, \mathbf{E}_{\text{ref}}, \mathbf{V}_{\text{ref}}, \mathbf{B}_{\text{ref}}\}$ (defined analogously for the generated images), and we concatenate them to the latent reference images, \mathbf{Z}_{ref} , as input to the network.

3D pose map conditioning. To obtain the 3D pose maps, $\mathbf{P}_{\text{ref/gen}}$ (illustrated in Figure 2), we use an off-the-shelf head tracker [83] that jointly fits a FLAME model [53] to each reference image. The tracker provides the shape, head pose, and expression blendshapes, along with camera intrinsics and extrinsics. We apply the blendshapes to a template model, \mathbf{T} , to recover the 3D models, $\mathbf{M}_{\text{ref}} = \{\mathbf{m}_{\text{ref}}^{(r)}\}_{r=1}^R$, corresponding to each reference image; we similarly define 3D models, $\mathbf{M}_{\text{gen}} = \{\mathbf{m}_{\text{gen}}^{(g)}\}_{g=1}^G$, for the generated images based on the desired head poses, expressions, and camera positions. Finally, we assign a texture to each vertex of $\mathbf{M}_{\text{ref/gen}}$, consisting of the 3D position of the corresponding vertex in the template mesh \mathbf{T} .

The 3D pose map is rendered by rasterizing the textures of $\mathbf{M}_{\text{ref/gen}}$ from the viewpoint of each reference and generated image:

$$\mathbf{p}_{\text{ref}}^{(r)} = \gamma \left[\text{RASTERIZE} \left(\mathbf{m}_{\text{ref}}^{(r)}, \mathbf{T}, \mathbf{\Pi}_{\text{ref}}^{(r)} \right) \right], \quad (2)$$

where $\mathbf{p}_{\text{ref}}^{(r)} \in \mathbf{P}_{\text{ref}}$ is the 3D pose map for the r th reference image, RASTERIZE performs rasterization of the reference

mesh using the associated 3D vertex position textures from the template mesh, and $\Pi_{\text{ref}}^{(r)}$ is the camera projection matrix given by the intrinsics and extrinsics. The function γ performs positional encoding [64] that maps the rasterized 3D vertex position at each pixel into a high-dimensional feature using sine and cosine functions (see the supplement for additional details). We render the 3D pose maps for the generated images in the same fashion.

Expression deformation map conditioning. To facilitate the generation of subtle expression changes, we explicitly condition the network with expression deformation maps, $\mathbf{E}_{\text{ref/gen}}$. We employ a procedure similar to that used for the 3D pose map, but we assign a different texture to each vertex of $\mathbf{M}_{\text{ref/gen}}$. Specifically, at each vertex, we calculate the 3D offset to the corresponding vertex of a 3D model that shares the same shape blendshapes, but uses the neutral expression blendshape. Then, we rasterize these vertex textures from the camera viewpoints of the reference and generated images. We omit the positional encoding step because the expression deformations have relatively low spatial frequencies [82].

View direction map and mask conditioning. For each reference and generated image, we encode the corresponding per-pixel ray directions into images, $\mathbf{V}_{\text{ref/gen}}$. We use ray directions, expressed relative to the reference frame of the first view, based on the estimated camera intrinsics and extrinsics from the tracker. An additional binary mask indicates whether the input image is a reference or generated image, and an outcropping mask identifies padded regions added to the reference images after center cropping around the head (see the supplement for additional details). All conditioning images are rendered at the latent image resolution and concatenated to the reference and generated latent images before input to the MMDM.

3.2. Generation

The first stage of our 4D avatar reconstruction procedure is an iterative image generation process. Given any number of reference images as input, we generate hundreds of novel views with a range of expressions.

Inference with stochastic I/O conditioning. The appearance of occluded head regions and expression-dependent features is ambiguous if only a few reference images are provided (e.g., hair on the back of the head, teeth covered by lips, wrinkles, etc.). Since the MMDM architecture can only take up to four reference images as input in a single forward pass, outputs of the model when using different reference images could have a very different likeness. To bypass this issue, we use a stochastic input–output (I/O)

Alg. 1: Inference with Stochastic I/O Conditioning

Input: Reference image latents and conditioning

$$\mathbf{Z}_{\text{ref}}, \mathbf{C}_{\text{ref}}, \mathbf{C}_{\text{gen}}$$

$$R = |\mathbf{Z}_{\text{ref}}| = |\mathbf{C}_{\text{ref}}|, G = |\mathbf{C}_{\text{gen}}|$$

G' : generated latents in each forward pass

Output: Generated image latents \mathbf{Z}_{gen}

$\mathbf{Z}_{\text{gen},T} \sim \mathcal{N}(\mathbf{0}, \mathbf{I})$ // sample noisy latents

for t in $(T, T - 1, \dots, 1)$ **do**

 // shuffle generated latents

$(\mathbf{Z}'_{\text{gen},t}, \mathbf{C}'_{\text{gen}}) \leftarrow \text{SHUFFLE}(\mathbf{Z}_{\text{gen},t}, \mathbf{C}_{\text{gen}})$

for i in $(0, \dots, G - 1)$ **do**

 // sample w/o replacement

$(\mathbf{Z}'_{\text{ref}}, \mathbf{C}'_{\text{ref}}) \leftarrow \text{RANDSAMPLE}((\mathbf{Z}_{\text{ref}}, \mathbf{C}_{\text{ref}}))$

 // sample next batch

$(\mathbf{Z}'_{\text{gen},t}, \mathbf{C}'_{\text{gen}}) \leftarrow (\mathbf{Z}_{\text{gen},t}, \mathbf{C}_{\text{gen}})[iG' + 1 : (i+1)G']$

 // predict noise

$\epsilon_{\text{id},t} = \text{MMDM}(\mathbf{Z}'_{\text{gen},t} | \mathbf{Z}'_{\text{ref}}, \mathbf{C}'_{\text{ref}}, \mathbf{C}'_{\text{gen}})$

 // apply DDIM step [80]

$$\mathbf{Z}'_{\text{gen},t-1} = \sqrt{\alpha_{t-1}} \left(\frac{\mathbf{Z}_{\text{gen},t} - \sqrt{1-\alpha_t} \epsilon_{\text{id},t}}{\sqrt{\alpha_t}} \right) + \sqrt{1-\alpha_{t-1}} \cdot \epsilon_{\text{id},t}$$

return $\mathbf{Z}_{\text{gen}} := \mathbf{Z}_{\text{gen},0}$

conditioning procedure where we pass a random subset of input reference images and generated images to the model at each diffusion timestep. This procedure has multiple benefits: (1) it improves the consistency of generated images; (2) it provides a mechanism to condition on tens to hundreds of reference images; and (3) it likewise enables generating hundreds of consistent output images.

A detailed description of inference using stochastic I/O conditioning is provided in Algorithm 1. We build on conventional denoising diffusion implicit model sampling [80] by adding an inner loop in each diffusion timestep where we shuffle the generated images and iterate over them in batches. Within this inner loop, we sample a batch of the generated images and a random subset of the reference images. Then, the model predicts the denoised generated latent images at the subsequent diffusion timestep using DDIM sampling. After iterating through all the generated images, we proceed to the next diffusion timestep, proceeding until all images have been completely denoised. Given a sufficient number of diffusion steps (we use 250), all reference and generated images participate jointly in the image generation process.

3.3. Robust 4D Avatar Reconstruction

Given the reference images, generated images, FLAME parameters, and camera views, we synthesize a 4D avatar. We build our representation based on GaussianAvatars [69], which uses a collection of 3D Gaussian splats attached to the triangles of a FLAME head mesh. Each Gaussian is linked to a specific parent triangle, with deformations mod-

eled by expression blendshapes that drive the mesh and triangle deformations. Additional Gaussians are added during optimization by splitting the existing Gaussians and assigning the new Gaussians to the same triangle. Different than GaussianAvatars, we remesh the FLAME head to achieve pixel-aligned vertices in UV space at 128×128 resolution. We capture fine-grained, expression-dependent deformations using a U-Net [73] that predicts a UV deformation map given the offsets in UV space due to the expression blendshape. We use our modified FLAME mesh, with an upper jaw mesh and an additional lower jaw mesh, which follows the design in GaussianAvatars. For more information please refer to the supplement.

To optimize the representation, we use the generated images alongside the sampled expression parameters, head poses, and camera poses. Additionally, we apply Laplacian regularization on the predicted deformation map and an L_2 regularization on the relative deformation and rotation of every Gaussian splat. We include an LPIPS [108] loss to improve robustness as proposed by previous work [31], where we increase λ_{LPIPS} linearly with the number of iterations. Additional details about the optimization and regularizers are included in the supplement.

4. Implementation

Training. We use a collection of monocular and multi-view videos to train our model: VFHQ [92], MEAD [88], Ava-256 [63] and Nersemble [50]. This amounts to 24.6k video sequences with a total number of 41.3M frames of 6317 diverse subjects. We use an off-the-shelf multi-view head tracker [83] to obtain 3DMM parameters along with a gaze estimator [1] to obtain the eye rotation from the video sequences. We train the model with the AdamW [59] optimizer, a learning rate of 10^{-4} , and batch size 64. We train the model for 80k iterations with $R = 1$, then train it for an additional 20k iterations with randomly chosen $R \leq 4$ for a total of 100k iterations. During training, we randomly drop-out all conditioning signals with a probability of 0.1, and we apply a classifier-free guidance [40] during inference. Training takes 2 weeks on $8 \times \text{H100}$ GPUs.

Sampling and 4D reconstruction. We generate $G = 840$ images using 250 DDIM steps with stochastic I/O conditioning, which takes around 4 hours on $4 \times \text{RTX6000}$ GPUs. 4D avatar reconstruction requires 100k iterations (≈ 4 hours on a single RTX6000 GPU). We provide additional optimization details in the supplement.

5. Experiments

We apply CAP4D to the tasks of self-reenactment and cross-reenactment and provide experimental results and comparisons to baselines. We also conduct an extensive set

of ablation studies to assess the impact of individual components of our method: the MMDM, stochastic I/O conditioning, and the 4D representation.

Baselines We implement and compare our method to baselines for single-view 4D avatar reconstruction: GAGA-vatar [19], Portrait4D-v2 [23], Real3D-Portrait [100] Voodoo3D [86]. We also include several multi-view reconstruction methods: DiffusionRig [24], FlashAvatar [91] and GaussianAvatars [69]. Last, we evaluate two ablated versions of our method—one without the MMDM (“w/o MMDM”; i.e., we reconstruct the avatar directly from the reference images) and one where the MMDM directly predicts the target frames (“MMDM only”).

5.1. Self-reenactment

We evaluate self-reenactment on nine multi-view capture sequences from the Nersemble [50] dataset. We hold out 4 of the 16 camera viewpoints for evaluation (each with 100 frames). From the remaining viewpoints, we select one (single), 10 (few), or 100 (many) reference images. Given the reference images, we assess how well each method reenacts the appearance of the evaluation images.

CAP4D significantly outperforms every baseline in the single- and few-image reconstruction categories (Tab. 1) in terms of photometric accuracy (PSNR, LPIPS), temporal consistency [62] (JOD) and identity preservation (using cosine similarity of identity embeddings [21]; CSIM). In the “many” reference image category, CAP4D achieves significantly higher LPIPS and CSIM than previous methods, indicating that avatars reconstructed with our method are sharper while improving identity preservation. Although FlashAvatar achieves competitive PSNR, its output images are blurrier than CAP4D (see Fig. 3), and hence it has a lower LPIPS score. We find that GaussianAvatars, FlashAvatar, and our 4D avatar trained without generated images (no-MMDM) tend to overfit to the reference views and do not generalize well to novel views. Our method improves with the number of reference images (see, e.g., CSIM), and by predicting the target frames directly (MMDM only), we achieve even higher visual quality (PSNR) at the cost of temporal consistency (JOD). Qualitatively CAP4D produces avatars with significantly higher visual fidelity than all baselines, especially for large deviations from the reference view (e.g., Fig. 3, row 1).

5.2. Cross-reenactment

To evaluate cross-reenactment, we select 10 reference images from the FFHQ [46] dataset. We pair five of the images with videos from VFHQ [92], which have a normal expression range, and we select five videos with more extreme expressions from Nersemble. The avatar is reconstructed from the reference image and the video drives its expressions.

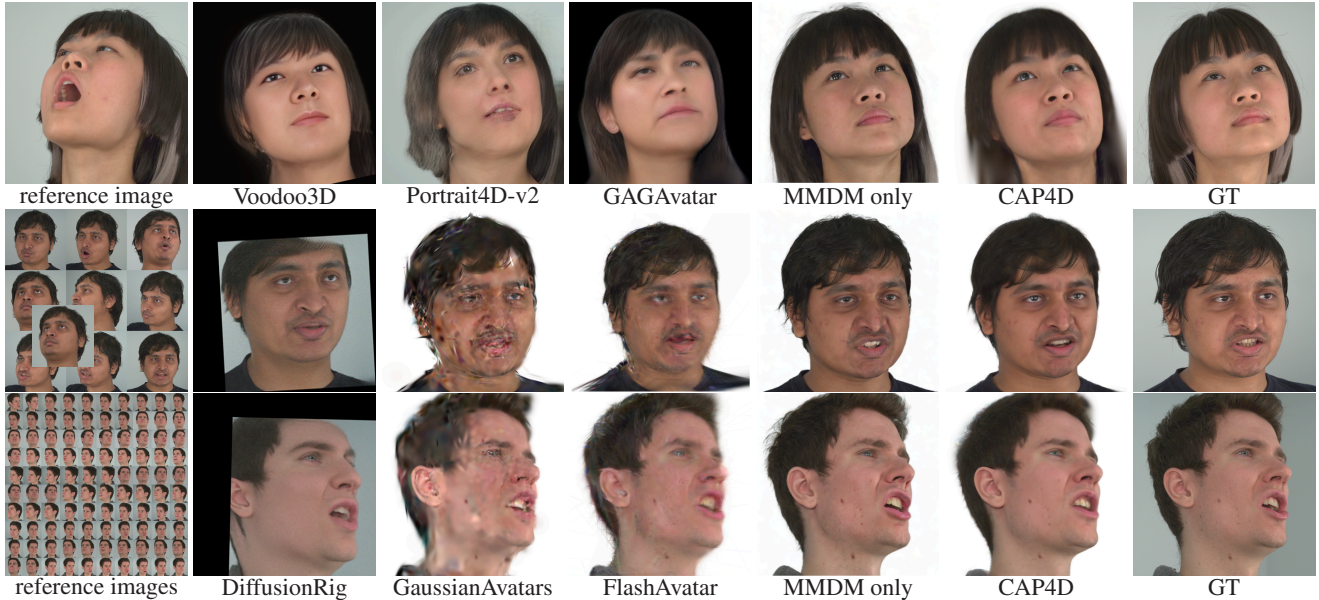


Figure 3. **Self-reenactment.** Our approach is more realistic than baseline methods for self-reenactment from a single reference image (row 1), 10 reference images (row 2) and 100 reference images (row 3). The MMDM output (MMDM only) produces the most realistic output at the cost of temporal consistency compared to our reconstructed 4D Avatar (CAP4D).

Method	single reference image				10 reference images				100 reference images			
	PSNR↑	LPIPS↓	CSIM↑	JOD↑	PSNR↑	LPIPS↓	CSIM↑	JOD↑	PSNR↑	LPIPS↓	CSIM↑	JOD↑
Voodoo3D [86]	19.05	0.381	0.282	4.782	16.55	0.450	0.475	3.89	16.61	0.446	0.435	3.86
GAGAvatar [19]	20.78	0.373	0.457	5.034	14.21	0.456	0.489	2.92	22.87	0.313	0.731	6.03
Real3D [100]	17.42	0.417	0.420	4.681	18.97	0.448	0.478	4.33	20.01	0.416	0.722	5.10
Portrait4D-v2 [23]	16.94	0.404	0.436	3.871								
MMDM only	21.82	0.317	0.632	5.397	17.05	0.404	0.578	4.19	19.07	0.333	0.758	4.97
CAP4D	21.69	0.311	0.633	5.672	23.82	0.270	0.804	6.06	24.12	0.266	0.803	6.14
					23.19	0.265	0.779	6.13	23.30	0.257	0.792	6.15

Table 1. **Single-image (left) and multi-image (right) self-reenactment results.** CAP4D outperforms previous methods across all metrics. Predicting images directly with the MMDM (MMDM only) trades off photometric quality (PSNR, LPIPS) and temporal consistency (JOD).

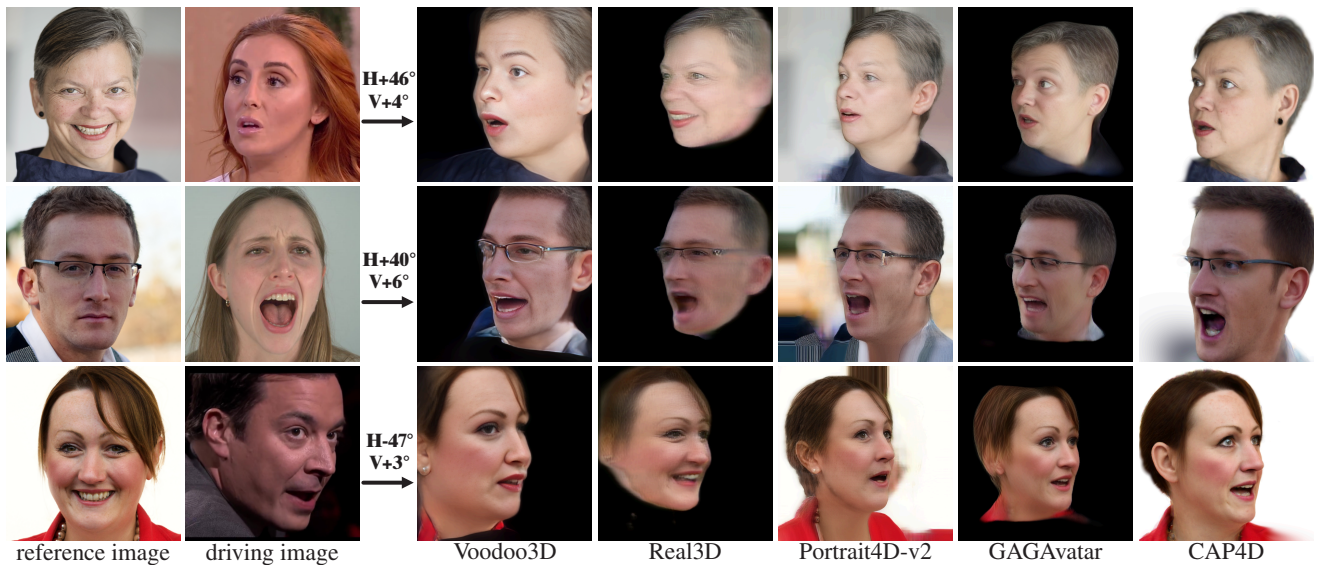


Figure 4. **Cross-reenactment.** Avatars are reconstructed from a single reference image (col. 1), and their expressions are driven by frames of a driving video (col. 2). The camera moves according to the indicated horizontal (H) and vertical (V) view angle. CAP4D faithfully recovers the driving expression and maintains the likeness of the reference subject from challenging view directions. It generates plausible results in occluded regions based on the reference image (e.g., earrings, row 1) and recovers high-frequency details (freckles, row 1).



Figure 5. **Extensions.** We demonstrate 4D appearance editing and relighting by applying CAP4D to images edited using off-the-shelf models [66, 109]. We also animate CAP4D avatars with a method that predicts 3DMM expressions from speech [94] (see supplement).

Method	CSIM \uparrow	human preference					Overall
		VQ	ET	3DS	TC		
Voodoo3D [86]	0.349	94%	94%	98%	99%	97%	
Real3D [100]	0.647	97%	90%	94%	94%	96%	
Portrait4D-v2 [23]	0.597	80%	73%	85%	89%	85%	
GAGAvatar [19]	0.606	75%	63%	74%	77%	74%	
CAP4D	0.634	—					

Table 2. **Cross-reenactment results.** We evaluate identity similarity (CSIM) and human preference based on visual quality (VQ), expression transfer (ET), 3D structure (3DS), temporal consistency (TC), and overall preference (Overall). The table reports the percentage of users (23 participants) who preferred CAP4D over the corresponding baseline in side-by-side comparisons.

We assess the results using the CSIM metric (Tab. 2) and in a user study, where 24 participants were presented with reference images, driving videos, and side-by-side videos generated with CAP4D and a baseline. Then, participants indicated their preference for each of the following criteria: visual quality, expression transfer accuracy, quality of 3D structure, temporal consistency, and overall preference.

The results of the user study (Tab. 2) show a clear preference toward CAP4D overall (74% versus the most competitive baseline), as well as across all other criteria. Although Real3D-Portrait [100] achieves slightly better performance in the CSIM metric, human users overwhelmingly prefer CAP4D to Real3D. Qualitative results (Fig. 4) indicate that CAP4D more faithfully captures the 3D appearance of the reference subject. Further, it preserves high-frequency detail better, is robust to large viewpoint changes, and produces 3D consistent video when other methods fail.

5.3. Ablations and Extensions

Ablation study. We investigate the design choices of our method relating to the MMDM, the stochastic sampling strategy, and the 4D reconstruction stage in Tab. 3. All ablations are conducted on the self-reenactment task with 10 reference images. Please refer to the supplement for more ablations and qualitative comparisons.

(MMDM) We ablate the expression deformation map (w/o expr) and view direction conditioning (w/o ray) after training the model for 30k steps. We find that the expression deformation map has a significant impact on photometric quality while the impact of view direction is less significant. **(Stochastic I/O sampling)** We directly predict the evaluation frames (MMDM-only) with and without stochastic

Category	Ablation	PSNR \uparrow	LPIPS \downarrow	CSIM \uparrow	JOD \uparrow
MMDM	w/o expr	21.64	0.320	0.669	5.43
	w/o ray	22.66	0.315	0.665	5.59
	Ours	22.54	0.308	0.668	5.59
sampling	w/o stochastic	23.43	0.282	0.755	5.92
	Ours	23.82	0.270	0.779	6.06
4D rep.	w/o U-Net	21.25	0.327	0.617	5.63
	w/o LPIPS	21.75	0.400	0.615	5.63
	Ours	21.69	0.311	0.633	5.67

Table 3. **Ablation study.** We assess the impact of removing the expression maps, view ray conditioning, stochastic I/O conditioning, and the deformation U-Net and LPIPS reconstruction loss.

sampling (w/o stochastic) with 10 reference frames. Tab. 3 shows that the stochastic sampling strategy improves the PSNR, CSIM, and JOD. **(4D avatar fitting)** We ablate our U-Net, which predicts expression-dependent deformations of the 3D Gaussians (“no U-Net”); without this component we see a decrease in PSNR and LPIPS due to a reduced capability to model effects such as wrinkles. We also ablate the LPIPS loss—removing it improves PSNR but at a cost to LPIPS and perceptual image equality.

Extensions. We demonstrate text-to-4D avatars generation by leveraging off-the-shelf image generation models such as Midjourney (Fig. 1). Similarly, we can extend any 2D face editing model to 4D by generating avatars from an edited reference image. We show virtual make-up and relighting examples in Fig. 5. Lastly, we exhibit speech-driven animation of a CAP4D avatar using an off-the-shelf FLAME-based [94] (see videos in the supplement).

6. Discussion

We see multiple promising avenues for future work. Currently, generation is time-consuming (up to 8 hours), and while the 3DMM is convenient to animate the avatar, it does not model certain effects (e.g., tongue or hair motion). Future extensions could enable animation without 3DMMs and improve appearance modeling through controllable lighting (e.g., similar to Saito et al. [74]). Finally, our method could be extended to model the full body.

Ethics statement. Digital human avatars are important to many applications, but can also be misused. We encourage responsible use of this technology (see Hancock and Bailenson [39] for an extended discussion).

Acknowledgements. DBL acknowledges support from LG Electronics, the Natural Sciences and Engineering Research Council of Canada (NSERC) under the RGPIN, RTI, and Alliance programs, the Canada Foundation for Innovation, and the Ontario Research Fund. The authors also acknowledge computing support provided by the Vector Institute.

References

- [1] Ahmed A. Abdelrahman, Thorsten Hempel, Aly Khalifa, Ayoub Al-Hamadi, and Laslo Dinges. L2CS-Net : Fine-grained gaze estimation in unconstrained environments. In *Proc. ICFSP*, pages 98–102, 2023. 6, 5
- [2] Oleg Alexander, Mike Rogers, William Lambeth, Jen-Yuan Chiang, Wan-Chun Ma, Chuan-Chang Wang, and Paul Debevec. The digital Emily project: Achieving a photorealistic digital actor. *IEEE Comput. Graph. Appl.*, 30(4):20–31, 2010. 1
- [3] ShahRukh Athar, Zexiang Xu, Kalyan Sunkavalli, Eli Shechtman, and Zhixian Shu. RigNeRF: Fully controllable neural 3D portraits. In *Proc. CVPR*, 2022. 3
- [4] ShahRukh Athar, Shunsuke Saito, Zhengyu Yang, Stanislav Pidhorsky, and Chen Cao. Bridging the gap: Studio-like avatar creation from a monocular phone capture. In *Proc. ECCV*, 2024. 3
- [5] Sherwin Bahmani, Xian Liu, Wang Yifan, Ivan Skorokhodov, Victor Rong, Ziwei Liu, Xihui Liu, Jeong Joon Park, Sergey Tulyakov, Gordon Wetzstein, et al. TC4D: Trajectory-conditioned text-to-4D generation. In *Proc. ECCV*, 2024. 3
- [6] Sherwin Bahmani, Ivan Skorokhodov, Victor Rong, Gordon Wetzstein, Leonidas Guibas, Peter Wonka, Sergey Tulyakov, Jeong Joon Park, Andrea Tagliasacchi, and David B Lindell. 4D-fy: Text-to-4D generation using hybrid score distillation sampling. In *Proc. CVPR*, 2024. 3
- [7] Ziqian Bai, Feitong Tan, Zeng Huang, Kripasindhu Sarkar, Danhang Tang, Di Qiu, Abhimitra Meka, Ruofei Du, Mingsong Dou, Sergio Orts-Escolano, et al. Learning personalized high quality volumetric head avatars from monocular RGB videos. In *Proc. CVPR*, 2023. 3
- [8] Jason Baldrige, Jakob Bauer, Mukul Bhutani, Nicole Brichtova, Andrew Bunner, Kelvin Chan, Yichang Chen, Sander Dieleman, Yuqing Du, Zach Eaton-Rosen, et al. ImageGen 3. *arXiv preprint arXiv:2408.07009*, 2024. 3
- [9] Volker Blanz and Thomas Vetter. A morphable model for the synthesis of 3D faces. In *Proc. SIGGRAPH*, 1999. 1, 3
- [10] Andreas Blattmann, Tim Dockhorn, Sumith Kulal, Daniel Mendelevitch, Maciej Kilian, Dominik Lorenz, Yam Levi, Zion English, Vikram Voleti, Adam Letts, et al. Stable video diffusion: Scaling latent video diffusion models to large datasets. *arXiv preprint arXiv:2311.15127*, 2023. 1, 2
- [11] Andreas Blattmann, Robin Rombach, Huan Ling, Tim Dockhorn, Seung Wook Kim, Sanja Fidler, and Karsten Kreis. Align your latents: High-resolution video synthesis with latent diffusion models. In *Proc. CVPR*, 2023. 3
- [12] Tim Brooks, Bill Peebles, Connor Holmes, Will DePue, Yufei Guo, Li Jing, David Schnurr, Joe Taylor, Troy Luhman, Eric Luhman, et al. Video generation models as world simulators, 2024. 3
- [13] Adrian Bulat and Georgios Tzimiropoulos. How far are we from solving the 2D & 3D face alignment problem? (and a dataset of 230,000 3D facial landmarks). In *Proc. ICCV*, 2017. 5
- [14] Egor Burkov, Igor Pasechnik, Artur Grigorev, and Victor Lempitsky. Neural head reenactment with latent pose descriptors. In *Proc. CVPR*, 2020. 3
- [15] Chen Cao, Tomas Simon, Jin Kyu Kim, Gabe Schwartz, Michael Zollhoefer, Shun-Suke Saito, Stephen Lombardi, Shih-En Wei, Danielle Belko, Shoou-I Yu, et al. Authentic volumetric avatars from a phone scan. *ACM Trans. Graph.*, 41(4):1–19, 2022. 3
- [16] Haoxin Chen, Yong Zhang, Xiaodong Cun, Menghan Xia, Xintao Wang, Chao Weng, and Ying Shan. VideoCrafter2: Overcoming data limitations for high-quality video diffusion models. In *Proc. CVPR*, 2024. 3
- [17] Ken Chen, Sachith Seneviratne, Wei Wang, Dongting Hu, Sanjay Saha, Md Tarek Hasan, Sanka Rasnayaka, Tamasha Malepathirana, Mingming Gong, and Saman Halgamuge. AniFaceDiff: High-fidelity face reenactment via facial parametric conditioned diffusion models. *arXiv preprint arXiv:2406.13272*, 2024. 1
- [18] Xiyi Chen, Marko Mihajlovic, Shaofei Wang, Sergey Prokudin, and Siyu Tang. Morphable Diffusion: 3D-consistent diffusion for single-image avatar creation. In *Proc. CVPR*, 2024. 1, 3
- [19] Xuangeng Chu and Tatsuya Harada. Generalizable and animatable Gaussian head avatar. In *Proc. NeurIPS*, 2024. 3, 6, 7, 8, 5
- [20] Hang Dai, Nick Pears, William Smith, and Christian Duncan. Statistical modeling of craniofacial shape and texture. *Int. J. Comput. Vis.*, 128(2):547–571, 2020. 1
- [21] Jiankang Deng, Jia Guo, Jing Yang, Niannan Xue, Irene Kotsia, and Stefanos Zafeiriou. ArcFace: Additive angular margin loss for deep face recognition. *IEEE Transactions on Pattern Analysis and Machine Intelligence*, 44(10):5962–5979, 2022. 6
- [22] Yu Deng, Duomin Wang, Xiaohang Ren, Xingyu Chen, and Baoyuan Wang. Portrait4D: Learning one-shot 4D head avatar synthesis using synthetic data. In *Proc. CVPR*, 2024. 3
- [23] Yu Deng, Duomin Wang, and baoyuan Wang. Portrait4D-v2: Pseudo multi-view data creates better 4D head synthesizer. *arXiv*, 2024. 6, 7, 8
- [24] Zheng Ding, Xuaner Zhang, Zhihao Xia, Lars Jebe, Zhuowen Tu, and Xiuming Zhang. DiffusionRig: Learning personalized priors for facial appearance editing. In *Proc. CVPR*, 2023. 1, 6, 7
- [25] Michail Christos Doukas, Stefanos Zafeiriou, and Viktoriia Sharmanska. HeadGAN: One-shot neural head synthesis and editing. In *Proc. ICCV*, 2021. 3
- [26] Nikita Drobyshev, Jenya Chelishev, Taras Khakhulin, Aleksei Ivakhnenko, Victor Lempitsky, and Egor Zakharov.

- MegaPortraits: One-shot megapixel neural head avatars. In *Proc. ACM-MM*, 2022. 3
- [27] Patrick Esser, Sumith Kulal, Andreas Blattmann, Rahim Entezari, Jonas Müller, Harry Saini, Yam Levi, Dominik Lorenz, Axel Sauer, Frederic Boesel, et al. Scaling rectified flow transformers for high-resolution image synthesis. In *Proc. ICML*, 2024. 3
- [28] Yao Feng, Haiwen Feng, Michael J. Black, and Timo Bolkart. Learning an animatable detailed 3D face model from in-the-wild images. *ACM Transactions on Graphics (ToG)*, *Proc. SIGGRAPH*, 40(8), 2021. 3, 5
- [29] Yasutaka Furukawa, Carlos Hernández, et al. Multi-view stereo: A tutorial. *Found. Trends Comput. Graph. Vis.*, 9(1-2):1–148, 2015. 1
- [30] Guy Gafni, Justus Thies, Michael Zollhofer, and Matthias Nießner. Dynamic neural radiance fields for monocular 4D facial avatar reconstruction. In *Proc. CVPR*, 2021. 1, 3
- [31] Ruiqi Gao*, Aleksander Holynski*, Philipp Henzler, Arthur Brussee, Ricardo Martin-Brualla, Pratul P. Srinivasan, Jonathan T. Barron, and Ben Poole*. Cat3d: Create anything in 3d with multi-view diffusion models. *Proc. NeurIPS*, 2024. 1, 3, 4, 6, 2
- [32] Pablo Garrido, Levi Valgaerts, Chenglei Wu, and Christian Theobalt. Reconstructing detailed dynamic face geometry from monocular video. *ACM Trans. Graph.*, 32(6):1–10, 2013. 1
- [33] Simon Giebenhain, Tobias Kirschstein, Markos Georgopoulos, Martin Rünz, Lourdes Agapito, and Matthias Nießner. Learning neural parametric head models. In *Proc. CVPR*, 2023. 1
- [34] Simon Giebenhain, Tobias Kirschstein, Markos Georgopoulos, Martin Rünz, Lourdes Agapito, and Matthias Nießner. MonoNPHM: Dynamic head reconstruction from monocular videos. In *Proc. CVPR*, 2024. 3
- [35] Philip-William Grassal, Malte Prinzler, Titus Leistner, Carsten Rother, Matthias Nießner, and Justus Thies. Neural head avatars from monocular rgb videos. In *Proc. CVPR*, 2022. 3
- [36] Yuming Gu, Hongyi Xu, You Xie, Guoxian Song, Yichun Shi, Di Chang, Jing Yang, and Linjie Luo. DiffPortrait3D: Controllable diffusion for zero-shot portrait view synthesis. In *Proc. CVPR*, 2024. 1
- [37] Jianzhu Guo, Dingyun Zhang, Xiaoqiang Liu, Zhizhou Zhong, Yuan Zhang, Pengfei Wan, and Di Zhang. Live-Portrait: Efficient portrait animation with stitching and re-targeting control. *arXiv preprint arXiv:2407.03168*, 2024. 3
- [38] Yuwei Guo, Ceyuan Yang, Anyi Rao, Zhengyang Liang, Yaohui Wang, Yu Qiao, Maneesh Agrawala, Dahua Lin, and Bo Dai. AnimateDiff: Animate your personalized text-to-image diffusion models without specific tuning. In *Proc. ICLR*, 2024. 3
- [39] Jeffrey T. Hancock and Jeremy N. Bailenson. The social impact of deepfakes. *Cyberpsychology, Behavior, and Social Networking*, 24(3):149–152, 2021. PMID: 33760669. 8
- [40] Jonathan Ho and Tim Salimans. Classifier-free diffusion guidance. In *NeurIPS 2021 Workshop on Deep Generative Models and Downstream Applications*, 2021. 6
- [41] Yicong Hong, Kai Zhang, Jiuxiang Gu, Sai Bi, Yang Zhou, Difan Liu, Feng Liu, Kalyan Sunkavalli, Trung Bui, and Hao Tan. LRM: Large reconstruction model for single image to 3D. *arXiv preprint arXiv:2311.04400*, 2023. 3
- [42] Emiel Hoogeboom, Jonathan Heek, and Tim Salimans. simple diffusion: End-to-end diffusion for high resolution images. In *Proc. ICML*, 2023. 1
- [43] Liangxiao Hu, Hongwen Zhang, Yuxiang Zhang, Boyao Zhou, Boning Liu, Shengping Zhang, and Liqiang Nie. GaussianAvatar: Towards realistic human avatar modeling from a single video via animatable 3D Gaussians. In *Proc. CVPR*, 2024. 3
- [44] Alexandru Eugen Ichim, Sofien Bouaziz, and Mark Pauly. Dynamic 3D avatar creation from hand-held video input. *ACM Trans. Graph.*, 34(4):1–14, 2015. 1, 3
- [45] Tero Karras, Samuli Laine, and Timo Aila. A style-based generator architecture for generative adversarial networks. In *Proc. CVPR*, 2019. 1
- [46] Tero Karras, Samuli Laine, and Timo Aila. A style-based generator architecture for generative adversarial networks. *IEEE Transactions on Pattern Analysis & Machine Intelligence*, 43(12):4217–4228, 2021. 6
- [47] Bernhard Kerbl, Georgios Kopanas, Thomas Leimkühler, and George Drettakis. 3D Gaussian splatting for real-time radiance field rendering. *ACM Trans. Graph.*, 42(4):1–14, 2023. 3, 4
- [48] Taras Khakhulin, Vanessa Sklyarova, Victor Lempitsky, and Egor Zakharov. Realistic one-shot mesh-based head avatars. In *Proc. ECCV*, 2022. 3
- [49] Taekyung Ki, Dongchan Min, and Gyeongsu Chae. Learning to generate conditional tri-plane for 3D-aware expression controllable portrait animation. In *Proc. ECCV*, 2024. 3
- [50] Tobias Kirschstein, Shenhan Qian, Simon Giebenhain, Tim Walter, and Matthias Nießner. Nersemble: Multi-view radiance field reconstruction of human heads. *ACM Trans. Graph.*, 42(4):1–14, 2023. 1, 6, 3, 4, 5
- [51] Tobias Kirschstein, Simon Giebenhain, and Matthias Nießner. DiffusionAvatars: Deferred diffusion for high-fidelity 3D head avatars. In *Proc. CVPR*, 2024. 5
- [52] Zhengfei Kuang, Shengqu Cai, Hao He, Yinghao Xu, Hongsheng Li, Leonidas Guibas, and Gordon Wetstein. Collaborative video diffusion: Consistent multi-video generation with camera control. *arXiv preprint arXiv:2405.17414*, 2024. 3
- [53] Tianye Li, Timo Bolkart, Michael J Black, Hao Li, and Javier Romero. Learning a model of facial shape and expression from 4D scans. *ACM Trans. Graph.*, 36(6):194–1, 2017. 1, 4, 3
- [54] Xueting Li, Shalini De Mello, Sifei Liu, Koki Nagano, Umar Iqbal, and Jan Kautz. Generalizable one-shot 3D neural head avatar. *Proc. NeurIPS*, 2024. 3
- [55] Shanchuan Lin, Linjie Yang, Imran Saleemi, and Soumyadip Sengupta. Robust high-resolution video matting with temporal guidance, 2021. 1

- [56] Shanchuan Lin, Bingchen Liu, Jiashi Li, and Xiao Yang. Common diffusion noise schedules and sample steps are flawed. In *Proc. WACV*, pages 5392–5399, Los Alamitos, CA, USA, 2024. IEEE Computer Society. 1
- [57] Ruoshi Liu, Rundi Wu, Basile Van Hoorick, Pavel Tokmakov, Sergey Zakharov, and Carl Vondrick. Zero-1-to-3: Zero-shot one image to 3D object. In *Proc. CVPR*, 2023. 1
- [58] Stephen Lombardi, Tomas Simon, Gabriel Schwartz, Michael Zollhoefer, Yaser Sheikh, and Jason Saragih. Mixture of volumetric primitives for efficient neural rendering. *ACM Trans. Graph.*, 40(4):1–13, 2021. 1
- [59] Ilya Loshchilov and Frank Hutter. Decoupled weight decay regularization. In *Proc. ICLR*, 2019. 6
- [60] Shugao Ma, Tomas Simon, Jason Saragih, Dawei Wang, Yuecheng Li, Fernando De La Torre, and Yaser Sheikh. Pixel codec avatars. In *Proc. CVPR*, 2021. 3
- [61] Zhiyuan Ma, Xiangyu Zhu, Guo-Jun Qi, Zhen Lei, and Lei Zhang. OTAvatar: One-shot talking face avatar with controllable tri-plane rendering. In *Proc. CVPR*, 2023. 3
- [62] Rafał K. Mantiuk, Gyorgy Denes, Alexandre Chapiro, Anton Kaplanyan, Gizem Rufo, Romain Bachy, Trisha Lian, and Anjul Patney. FovVideoVDP: a visible difference predictor for wide field-of-view video. *ACM Trans. Graph.*, 40(4), 2021. 6
- [63] Julieta Martinez, Emily Kim, Javier Romero, Timur Bagautdinov, Shunsuke Saito, Shoou-I Yu, Stuart Anderson, Michael Zollhöfer, Te-Li Wang, Shaojie Bai, Chenghui Li, Shih-En Wei, Rohan Joshi, Wyatt Borsos, Tomas Simon, Jason Saragih, Paul Theodosis, Alexander Greene, Anjani Josyula, Silvio Mano Maeta, Andrew I. Jewett, Simon Venshtain, Christopher Heilman, Yueh-Tung Chen, Sidi Fu, Mohamed Ezzeldin A. Elshaer, Tingfang Du, Longhua Wu, Shen-Chi Chen, Kai Kang, Michael Wu, Youssef Emad, Steven Longay, Ashley Brewer, Hitesh Shah, James Booth, Taylor Koska, Kayla Haidle, Matt Andromalos, Joanna Hsu, Thomas Dauer, Peter Selednik, Tim Godisart, Scott Ardisson, Matthew Cipperly, Ben Humberston, Lon Farr, Bob Hansen, Peihong Guo, Dave Braun, Steven Krenn, He Wen, Lucas Evans, Natalia Fadeeva, Matthew Stewart, Gabriel Schwartz, Divam Gupta, Gyeongsik Moon, Kaiwen Guo, Yuan Dong, Yichen Xu, Takaaki Shiratori, Fabian Prada, Bernardo R. Pires, Bo Peng, Julia Buffalini, Autumn Trimble, Kevyn McPhail, Melissa Schoeller, and Yaser Sheikh. Codec Avatar Studio: Paired Human Captures for Complete, Driveable, and Generalizable Avatars. *NeurIPS Track on Datasets and Benchmarks*, 2024. 6, 5
- [64] Ben Mildenhall, Pratul P Srinivasan, Matthew Tancik, Jonathan T Barron, Ravi Ramamoorthi, and Ren Ng. NeRF: Representing scenes as neural radiance fields for view synthesis. *Commun. ACM.*, 65(1):99–106, 2021. 3, 5
- [65] Arsha Nagrani, Joon Son Chung, and Andrew Zisserman. VoxCeleb: A large-scale speaker identification dataset. In *Proc. Interspeech*, 2017. 1
- [66] Puntawat Ponglertnapakorn, Nontawat Tritrong, and Supasorn Suwajanakorn. DiFaReli: Diffusion face relighting. In *Proc. CVPR*, 2023. 8
- [67] Ben Poole, Ajay Jain, Jonathan T Barron, and Ben Mildenhall. DreamFusion: Text-to-3D using 2D diffusion. In *Proc. ICLR*, 2023. 3
- [68] Malte Prinzler, Egor Zakharov, Vanessa Sklyarova, Berna Kabadayi, and Justus Thies. Joker: Conditional 3D head synthesis with extreme facial expressions. *arXiv preprint arXiv:2410.16395*, 2024. 1, 3
- [69] Shenhan Qian, Tobias Kirschstein, Liam Schoneveld, Davide Davoli, Simon Giebenhain, and Matthias Nießner. GaussianAvatars: Photorealistic head avatars with rigged 3D Gaussians. In *Proc. CVPR*, 2024. 3, 4, 5, 6, 7, 10
- [70] Daniel Rebain, Mark Matthews, Kwang Moo Yi, Dmitry Lagun, and Andrea Tagliasacchi. LOLNeRF: Learn from one look. In *Proc. CVPR*, 2022. 3
- [71] Yurui Ren, Ge Li, Yuanqi Chen, Thomas H Li, and Shan Liu. Pirenderer: Controllable portrait image generation via semantic neural rendering. In *Proc. ICCV*, 2021. 3
- [72] Robin Rombach, Andreas Blattmann, Dominik Lorenz, Patrick Esser, and Björn Ommer. High-resolution image synthesis with latent diffusion models. In *Proc. CVPR*, 2022. 3, 4
- [73] Olaf Ronneberger, Philipp Fischer, and Thomas Brox. U-Net: Convolutional networks for biomedical image segmentation, 2015. 6, 4
- [74] Shunsuke Saito, Gabriel Schwartz, Tomas Simon, Junxuan Li, and Giljoo Nam. Relightable gaussian codec avatars. In *Proc. CVPR*, 2024. 8
- [75] Shaul Salomon, Gideon Avigad, Alex Goldvard, and Oliver Schütze. PSA – a new scalable space partition based selection algorithm for MOEAs. In *Proc. EVOLVE*, 2013. 3, 4
- [76] Zhijing Shao, Zhaolong Wang, Zhuang Li, Duotun Wang, Xiangru Lin, Yu Zhang, Mingming Fan, and Zeyu Wang. SplattingAvatar: Realistic real-time human avatars with mesh-embedded Gaussian splatting. In *Proc. CVPR*, 2024. 3
- [77] Ruoxi Shi, Hansheng Chen, Zhuoyang Zhang, Minghua Liu, Chao Xu, Xinyue Wei, Linghao Chen, Chong Zeng, and Hao Su. Zero123++: a single image to consistent multi-view diffusion base model. *arXiv preprint arXiv:2310.15110*, 2023. 3
- [78] Yichun Shi, Peng Wang, Jianglong Ye, Long Mai, Kejie Li, and Xiao Yang. MVDream: Multi-view diffusion for 3D generation. In *Proc. ICLR*, 2023. 1, 3
- [79] Aliaksandr Siarohin, Stéphane Lathuilière, Sergey Tulyakov, Elisa Ricci, and Nicu Sebe. First order motion model for image animation. *Proc. NeurIPS*, 2019. 1, 3
- [80] Jiaming Song, Chenlin Meng, and Stefano Ermon. Denoising diffusion implicit models. In *Proc. ICLR*, 2020. 3, 5
- [81] Jingxiang Sun, Bo Zhang, Ruizhi Shao, Lizhen Wang, Wen Liu, Zhenda Xie, and Yebin Liu. DreamCraft3D: Hierarchical 3D generation with bootstrapped diffusion prior. In *Proc. ICLR*, 2024. 3
- [82] Matthew Tancik, Pratul Srinivasan, Ben Mildenhall, Sara Fridovich-Keil, Nithin Raghavan, Utkarsh Singhal, Ravi Ramamoorthi, Jonathan Barron, and Ren Ng. Fourier features let networks learn high frequency functions in low dimensional domains. *Proc. NeurIPS*, 2020. 5, 1

- [83] Felix Taubner, Prashant Raina, Mathieu Tuli, Eu Wern Teh, Chul Lee, and Jinmiao Huang. 3D face tracking from 2D video through iterative dense uv to image flow. In *Proc. CVPR*, 2024. 1, 4, 6, 5
- [84] Ayush Tewari, Justus Thies, Ben Mildenhall, Pratul Srinivasan, Edgar Tretschk, Wang Yifan, Christoph Lassner, Vincent Sitzmann, Ricardo Martin-Brualla, Stephen Lombardi, et al. Advances in neural rendering. *Comput. Graph. Forum*, 41(2):703–735, 2022. 1
- [85] Linrui Tian, Qi Wang, Bang Zhang, and Liefeng Bo. EMO: Emote portrait alive-generating expressive portrait videos with audio2video diffusion model under weak conditions. *arXiv preprint arXiv:2402.17485*, 2024. 1
- [86] Phong Tran, Egor Zakharov, Long-Nhat Ho, Anh Tuan Tran, Liwen Hu, and Hao Li. VOODOO 3D: Volumetric portrait disentanglement for one-shot 3D head reenactment. *Proc. CVPR*, 2024. 3, 6, 7, 8
- [87] Alex Trevithick, Matthew Chan, Michael Stengel, Eric Chan, Chao Liu, Zhiding Yu, Sameh Khamis, Manmohan Chandraker, Ravi Ramamoorthi, and Koki Nagano. Real-time radiance fields for single-image portrait view synthesis. *ACM Trans. Graph.*, 42(4):1–15, 2023. 3
- [88] Kaisiyuan Wang, Qianyi Wu, Linsen Song, Zhuoqian Yang, Wayne Wu, Chen Qian, Ran He, Yu Qiao, and Chen Change Loy. MEAD: A large-scale audio-visual dataset for emotional talking-face generation. In *Proc. ECCV*, 2020. 6, 5
- [89] Ting-Chun Wang, Arun Mallya, and Ming-Yu Liu. One-shot free-view neural talking-head synthesis for video conferencing. In *Proc. CVPR*, 2021. 3
- [90] Daniel Watson, William Chan, Ricardo Martin Brualla, Jonathan Ho, Andrea Tagliasacchi, and Mohammad Norouzi. Novel view synthesis with diffusion models. In *Proc. ICLR*, 2023. 3
- [91] Jun Xiang, Xuan Gao, Yudong Guo, and Juyong Zhang. FlashAvatar: High-fidelity head avatar with efficient gaussian embedding. In *Proc. CVPR*, 2024. 1, 3, 6, 7, 5
- [92] Liangbin Xie, Xintao Wang, Honglun Zhang, Chao Dong, and Ying Shan. VFHQ: A high-quality dataset and benchmark for video face super-resolution. In *Proc. CVPR*, 2022. 1, 6, 5
- [93] You Xie, Hongyi Xu, Guoxian Song, Chao Wang, Yichun Shi, and Linjie Luo. X-portrait: Expressive portrait animation with hierarchical motion attention. In *Proc. SIGGRAPH*, 2024. 1
- [94] Jinbo Xing, Menghan Xia, Yuechen Zhang, Xiaodong Cun, Jue Wang, and Tien-Tsin Wong. CodeTalker: Speech-driven 3D facial animation with discrete motion prior. In *Proc. CVPR*, pages 12780–12790, 2023. 8
- [95] Sicheng Xu, Jiaolong Yang, Dong Chen, Fang Wen, Yu Deng, Yunde Jia, and Xin Tong. Deep 3D portrait from a single image. In *Proc. CVPR*, 2020. 3
- [96] Sicheng Xu, Guojun Chen, Yu-Xiao Guo, Jiaolong Yang, Chong Li, Zhenyu Zang, Yizhong Zhang, Xin Tong, and Baining Guo. Vasa-1: Lifelike audio-driven talking faces generated in real time. *arXiv preprint arXiv:2404.10667*, 2024. 3
- [97] Yuelang Xu, Benwang Chen, Zhe Li, Hongwen Zhang, Lizhen Wang, Zerong Zheng, and Yebin Liu. Gaussian head avatar: Ultra high-fidelity head avatar via dynamic Gaussians. In *Proc. CVPR*, 2024. 3
- [98] Zhongcong Xu, Jianfeng Zhang, Jun Hao Liew, Wenqing Zhang, Song Bai, Jiashi Feng, and Mike Zheng Shou. PV3D: A 3D generative model for portrait video generation. In *Proc. ICLR*, 2023. 3
- [99] Haotian Yang, Hao Zhu, Yanru Wang, Mingkai Huang, Qiu Shen, Ruigang Yang, and Xun Cao. FaceScape: a large-scale high quality 3D face dataset and detailed riggable 3D face prediction. In *Proc. CVPR*, 2020. 1, 3
- [100] Zhenhui Ye, Tianyun Zhong, Yi Ren, Jiaqi Yang, Weichuang Li, Jiawei Huang, Ziyue Jiang, Jinzheng He, Rongjie Huang, Jinglin Liu, et al. Real3D-Portrait: One-shot realistic 3D talking portrait synthesis. In *Proc. ICLR*, 2024. 3, 6, 7, 8
- [101] Fei Yin, Yong Zhang, Xiaodong Cun, Mingdeng Cao, Yanbo Fan, Xuan Wang, Qingyan Bai, Baoyuan Wu, Jue Wang, and Yujiu Yang. StyleHEAT: One-shot high-resolution editable talking face generation via pre-trained stylegan. In *Proc. ECCV*. Springer, 2022. 3
- [102] Wangbo Yu, Yanbo Fan, Yong Zhang, Xuan Wang, Fei Yin, Yunpeng Bai, Yan-Pei Cao, Ying Shan, Yang Wu, Zhongqian Sun, et al. NOFA: NeRF-based one-shot facial avatar reconstruction. In *Proc. SIGGRAPH*, 2023. 3
- [103] Egor Zakharov, Aliaksandra Shysheya, Egor Burkov, and Victor Lempitsky. Few-shot adversarial learning of realistic neural talking head models. In *Proc. ICCV*, 2019. 3
- [104] Egor Zakharov, Aleksei Ivakhnenko, Aliaksandra Shysheya, and Victor Lempitsky. Fast bi-layer neural synthesis of one-shot realistic head avatars. In *Proc. ECCV*, 2020.
- [105] Bowen Zhang, Chenyang Qi, Pan Zhang, Bo Zhang, HsiangTao Wu, Dong Chen, Qifeng Chen, Yong Wang, and Fang Wen. MetaPortrait: Identity-preserving talking head generation with fast personalized adaptation. In *Proc. CVPR*, 2023. 3
- [106] Bowen Zhang, Yiji Cheng, Chunyu Wang, Ting Zhang, Jiaolong Yang, Yansong Tang, Feng Zhao, Dong Chen, and Baining Guo. RodinHD: High-fidelity 3D avatar generation with diffusion models. *arXiv preprint arXiv:2407.06938*, 2024. 3
- [107] Fan Zhang, Valentin Bazarevsky, Andrey Vakunov, Andrei Tkachenka, George Sung, Chuo-Ling Chang, and Matthias Grundmann. MediaPipe hands: On-device real-time hand tracking, 2020. 5
- [108] Richard Zhang, Phillip Isola, Alexei A Efros, Eli Shechtman, and Oliver Wang. The unreasonable effectiveness of deep features as a perceptual metric. In *Proc. CVPR*, 2018. 6, 4
- [109] Yuxuan Zhang, Lifu Wei, Qing Zhang, Yiren Song, Jiaming Liu, Huaxia Li, Xu Tang, Yao Hu, and Haibo Zhao. Stable-Makeup: When real-world makeup transfer meets diffusion model, 2024. 8
- [110] Xiaochen Zhao, Lizhen Wang, Jingxiang Sun, Hongwen Zhang, Jinli Suo, and Yebin Liu. HAvatar: High-fidelity

head avatar via facial model conditioned neural radiance field. *ACM Trans. Graph.*, 43(1):1–16, 2023. 3

- [111] Yufeng Zheng, Victoria Fernández Abrevaya, Marcel C Bühler, Xu Chen, Michael J Black, and Otmar Hilliges. I M avatar: Implicit morphable head avatars from videos. In *Proc. CVPR*, 2022. 3
- [112] Yufeng Zheng, Wang Yifan, Gordon Wetzstein, Michael J Black, and Otmar Hilliges. PointAvatar: Deformable point-based head avatars from videos. In *Proc. CVPR*, 2023. 3
- [113] Zhenglin Zhou, Fan Ma, Hehe Fan, and Yi Yang. Headstudio: Text to animatable head avatars with 3D Gaussian splatting. In *Proc. ECCV*, 2024. 3
- [114] Yiyu Zhuang, Hao Zhu, Xusen Sun, and Xun Cao. MoFaNeRF: Morphable facial neural radiance field. In *Proc. ECCV*, 2022. 3
- [115] Wojciech Zielonka, Timo Bolkart, and Justus Thies. Instant volumetric head avatars. *Proc. CVPR*, 2022. 1, 3
- [116] Wojciech Zielonka, Timo Bolkart, and Justus Thies. Towards metrical reconstruction of human faces. In *Proc. ECCV*, 2022. 1, 3

CAP4D: Creating Animatable 4D Portrait Avatars with Morphable Multi-View Diffusion Models

Supplementary Material

This document includes supplementary implementation details and results. We provide implementation details related to the morphable multi-view diffusion model (MMDM), 3D morphable model (3DMM), 4D avatar, datasets, and evaluation procedures; we also provide additional evaluations and ablation studies. We encourage the reader to inspect our visual results, comparisons with other models, and additional visualizations in the accompanying project page felixtaubner.github.io/cap4d.

A. MMDM Implementation

A.1. Model architecture

Our model is based on Stable Diffusion 2.1 [10] and illustrated in Fig. S1. We remove all cross-attention layers and replace the 2D self-attention layers after 2D residual blocks with 3D attention layers to create the multi-view diffusion model. Following Gao et al. [31], we only modify the 2D self-attention for layers with dimensions 32×32 , 16×16 , and 8×8 . We also adjust the first convolutional layer of the model to accommodate the additional conditioning channels and, where possible, initialize all layers with pre-trained weights.

During training, we update all model parameters and follow Stable Diffusion with the following adjustments. First, we shift the signal-to-noise ratio of the noise schedule by $\log(\sqrt{N})$. Adjusting the noise schedule provides more diffusion steps for the model to learn coarse structures in the generated images [31, 42]. Second, we found that adjusting the noise schedule to have zero terminal SNR is vital to avoid artifacts in the background [56]. Our latent diffusion model has a total of 815M parameters. We use classifier free guidance weight of 2 during sampling.

A.2. Conditioning

The MMDM takes as input a set of reference or generated images, and each set is paired with five additional sets of conditioning images (illustrated in Fig. S2): $\mathbf{V}_{\text{ref/gen}}$, view direction maps containing per-pixel view directions in world coordinates; $\mathbf{P}_{\text{ref/gen}}$, 3D pose maps with rasterized vertex positions of the 3DMM template mesh; $\mathbf{E}_{\text{ref/gen}}$, expression deformation maps with rasterized vertex deformation vectors; and $\mathbf{B}_{\text{ref/gen}}$, pairs of binary masks that indicate (1) outcropped areas that are padded with white pixels and (2) whether the input is a reference or generated image.

Preprocessing steps and binary masks. To create the reference conditioning images, we first obtain FLAME [53] parameters, camera intrinsic parameters, and extrinsic parameters using the 3DMM estimator of Taubner et al. [83]. To create the generated conditioning images, we sample the FLAME parameters as described in the following section.

We crop the reference images by fitting a bounding box around the vertices of the 3DMM projected onto the camera image plane. Then, we find the smallest square bounding box that encloses the original bounding box (centered at the same location) and enlarge the result by 30% to include the hair, neck, and shoulders; this bounding box is used for cropping. We resize the cropped image to 512×512 resolution, adjust the camera intrinsics to be consistent with this cropped frame, and remove the background using an off-the-shelf background matting model [55].

Sometimes, the bounding box used to crop the image extends outside the image boundaries. To perform outcropping in such regions, we pad the image with white pixels, and we flag these regions using a binary outcropping mask, where all outcropped areas are indicated with white pixels. The MMDM is conditioned on $\mathbf{B}_{\text{ref/gen}}$, consisting of the outcropping masks and binary masks that indicate whether the input is a reference or generated image.

View direction conditioning. We use the camera intrinsic and extrinsic parameters to compute view conditioning images, $\mathbf{V}_{\text{ref/gen}}$, containing the view direction for each pixel in world coordinates. The world coordinates are computed relative to the first reference view, which is positioned at the origin of the coordinate system with its rotation matrix set to the identity.

3D pose and expression deformation conditioning. As described in the main text, we obtain the 3D pose map $\mathbf{P}_{\text{ref/gen}}$ by texturing the vertices of the tracked 3DMM model with the 3D vertex positions of the 3DMM template mesh \mathbf{T} . We rasterize these vertex positions and encode the values using a periodic positional encoding [82]:

$$\gamma(p) = (\sin(2^0 p), \cos(2^0 p), \dots, \sin(2^{L-1} p), \cos(2^{L-1} p)), \quad (3)$$

where p is the 3D vertex position texture, and $L = 7$ is the number of encoding frequencies. This results in 42 positional encoding channels. We compute $\mathbf{E}_{\text{ref/gen}}$ in a similar fashion by rasterizing the 3D deformations caused by the expression blendshape parameters ($\mathcal{E}(\phi)$), but we omit the positional encoding.

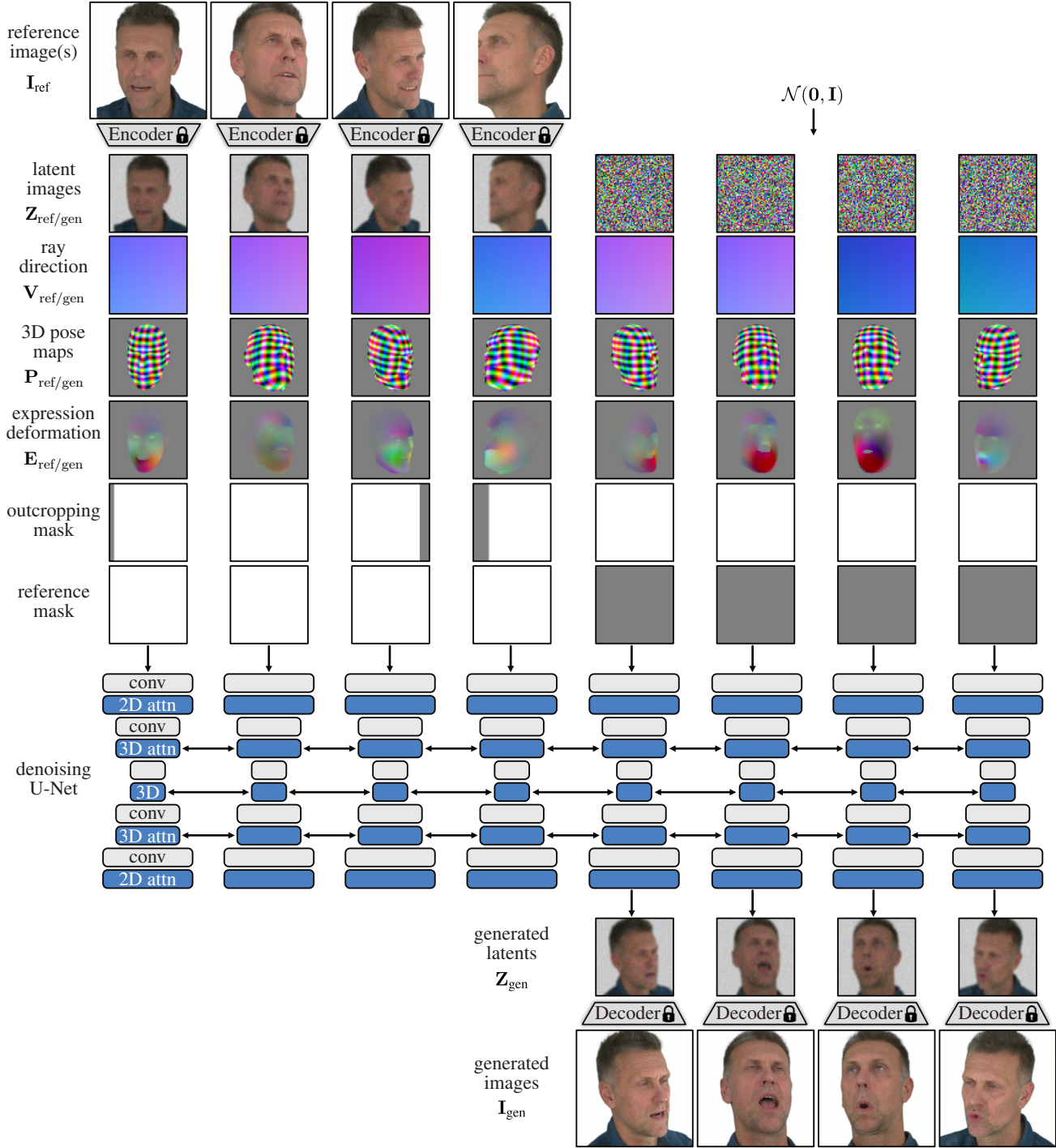


Figure S1. **MMDM architecture.** Our model is initialized from Stable Diffusion 2.1 [10], and we adapt the architecture for multi-view generation following CAT3D [31]. We use a pre-trained image encoder to map the input images into the latent space, and we use the latent diffusion model to process eight images in parallel. We replace 2D attention layers after 2D residual blocks with 3D attention to share information between frames. The model is conditioned using images that provide information such as head pose, expression, and camera view. The denoised latent image is decoded using a pre-trained decoder.

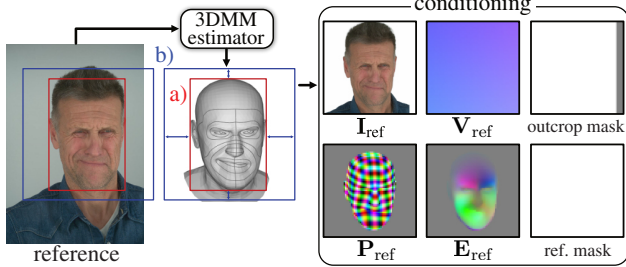


Figure S2. **MMDM conditioning.** We preprocess each reference image based on the estimated 3DMM model. We obtain a tight-fitting bounding box around the head region (a), which is squared and enlarged (b). We crop the image to the square bounding box and remove the background. Then, we update camera intrinsics to the updated crop and obtain the conditioning images \mathbf{V}_{ref} (ray directions), \mathbf{P}_{ref} (3D pose map), \mathbf{E}_{ref} (expression deformation map) and outcrop mask. We follow the same process for generated images.

A.3. MMDM sampling

We follow a fixed sampling procedure to obtain novel generated views and 3DMM parameters as illustrated in Fig. S3. We begin by sampling a set of G generated camera views, where each view is rotated around the center of the head with a randomly sampled azimuth ψ and elevation angle θ (we set the view aligned straight on with the face to have zero azimuth and zero elevation). The camera is kept at the same distance from the head as the first reference view. The values ψ and θ are uniformly sampled to be within an ellipse (red line, Fig. S3):

$$\left(\frac{\psi}{\psi_{\max}}\right)^2 + \left(\frac{\theta}{\theta_{\max}}\right)^2 < 1, \quad (4)$$

where $\psi_{\max} = 55^\circ$ and $\theta_{\max} = 20^\circ$.

Expression database. We select a unique expression parameter for each camera view from our expression database. The database is created using a diversity-promoting sampling scheme (implemented in the `diversipy` software package [75]) that partitions the space of expressions obtained from all frames of the Nersemble [50] dataset into $G = 840$ dissimilar subsets with a representative sample for each subset. To determine the distance between each expression sample, we use Euclidean distance in expression parameter space $\phi \in \mathbb{R}^{65}$, where each dimension is weighted by the maximum vertex displacement of the corresponding blendshape.

B. FLAME 3DMM Implementation

The FLAME representation [53] consists of $N_v = 5023$ vertices, which are controlled by identity shape parameters β , expression shape parameters ϕ , and skeletal joint

poses through linear blend skinning. We ignore the jaw pose and use the FLAME2023 model, which includes deformations due to jaw rotation within the expression blendshapes. Overall, there are $\beta \in \mathbb{R}^{150}$ identity shape parameters and $\phi \in \mathbb{R}^{65}$ expression parameters. To model eye rotation, we use one joint rotation for both eyes. Each vertex position is determined by adding expression and identity shape offsets to the template mesh \mathbf{T} , and the offsets are computed using the expression and identity shape parameters and the corresponding linear bases, \mathcal{E} and \mathcal{S} :

$$\mathbf{m} = \mathbf{T} + \mathcal{E}(\phi) + \mathcal{S}(\beta). \quad (5)$$

We use an edited version of the FLAME template mesh to create the conditioning signals used by the MMDM. More precisely, we manually position a spherical mesh inside the mouth region and behind the lip to represent the upper jaw. This sphere is static and unaffected by the expression shape parameters ϕ . We remove the lower neck vertices and limit the conditioning model to the head region.

For the representation used by the 4D avatar, we add a spherical mesh to model the lower jaw. This sphere is placed similarly to the upper jaw mesh, but it is rigged to move with the jaw joint. We compute the jaw rotation heuristically by tracking the deformation of a specific vertex on the lower jaw relative to the jaw joint position obtained from the FLAME model. We adopt the UV mapping provided by previous work [28] and modify it manually to add textures for the upper and lower jaw meshes.

C. 4D Avatar Implementation

Our 4D avatar model is based on GaussianAvatars [69] with a few modifications to make it more robust to generated views. We describe these changes in the following and illustrate the approach in Fig. S4.

Deformation model. We disable the per-frame fine-tuning of FLAME parameters used by GaussianAvatars during training as we find that it leads to overfitting. To correct inaccuracies in the underlying 3DMM, we instead use a U-Net to deform the mesh with expression-dependent deformations.

The input to the U-Net consists of UV maps that encode the expression deformations and positional encodings of UV map pixel locations. To compute the expression deformation map, we first remesh the FLAME head to achieve pixel-aligned vertices in UV space at a 128×128 resolution. Then, we rasterize the deformations caused by the expression parameters $\mathcal{E}(\phi)$ into UV space. We obtain a positional encoding of the UV space by encoding the UV coordinates with the same periodic functions as in Eq. (4), where we set the number of frequencies to $L = 6$ and the coordinate p to the UV-space coordinate of each pixel, leading to a total

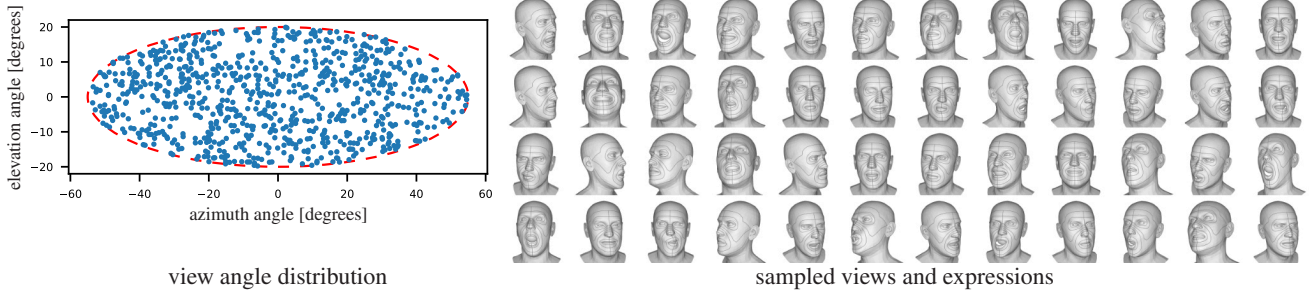


Figure S3. **3DMM Sampling.** To generate novel views we uniformly sample in azimuth and elevation (left). For each camera view, we select unique expression parameters from our expression database, which is obtained from the Nersemble dataset [50] following a diversity-promoting sampling scheme [75]. A subset of the sampled expressions and views are visualized on the right.

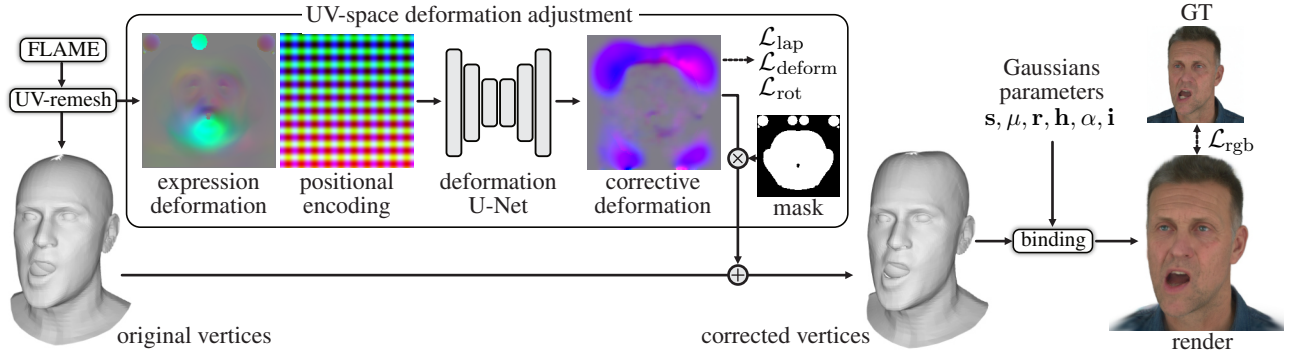


Figure S4. **Overview of 4D Avatar Model.** Our 4D representation incorporates multiple improvements to the GaussianAvatars [69] model. First, we re-mesh the FLAME topology so that each vertex corresponds to a pixel in the UV space. Then, we input the UV-space deformations caused by the expression blendshapes and a UV-space positional encoding into a deformation U-Net. This U-Net outputs corrective deformations, which, after masking, are added to the remeshed FLAME output. Following Qian et al. [69], the Gaussians are parameterized by a scale s , local position μ , local rotation r , spherical harmonics coefficients h , opacity α , and parent triangle i . We apply regularizers to the output of the U-Net, and we add an LPIPS penalty to the photometric loss \mathcal{L}_{rgb} .

number of 24 encoding channels. The positional encoding is concatenated to the UV-space expression deformation and processed by a 6-layer U-Net [73].

The U-Net outputs a 3-channel deformation map, D_{uv} , (see Figure S4) indicating the expression-dependent deformation correction. We mask this deformation to prevent deformations in static areas such as the back of the head and lower neck. To obtain the final vertex positions, we add these deformations to the vertices produced by the FLAME model.

During training, we use multiple regularizers to prevent motion artifacts. First, we apply a weight decay of 2×10^{-3} on the U-Net weights; second, we use an L2 loss $\mathcal{L}_{lap} = \|\Delta D_{uv}\|_2^2$ on the Laplacian of the deformation map; last we append an L2 loss on the relative deformation and rotation of each Gaussian \mathcal{L}_{deform} and \mathcal{L}_{rot} . We logarithmically decrease the learning rate of this network from 10^{-5} to 10^{-7} during training.

LPIPS loss. To make the reconstruction more robust to inconsistencies in the generated views, we add an LPIPS [108] loss to the existing photometric loss from GaussianAvatars [69] and weight it against the other term:

$$\mathcal{L}_{rgb} = \lambda_{LPIPS} \mathcal{L}_{LPIPS} + (1 - \lambda_{LPIPS}) \mathcal{L}_{rgb,GA}, \quad (6)$$

where λ_{LPIPS} is the weighting of LPIPS loss, which we linearly increase from 0 to 0.9 during training. $\mathcal{L}_{rgb,GA}$ is the original photometric loss from GaussianAvatars. We also include their scaling and positional losses $\mathcal{L}_{scaling}$ and $\mathcal{L}_{position}$, resulting in the modified total loss function:

$$\mathcal{L} = \mathcal{L}_{rgb} + \lambda_{deform} \mathcal{L}_{deform} + \lambda_{rot} \mathcal{L}_{rot} + \mathcal{L}_{scaling} + \mathcal{L}_{position}, \quad (7)$$

where $\lambda_{deform} = 0.4$ and $\lambda_{rot} = 0.005$ are the weights for the corresponding losses. For more information on these loss functions, we refer to GaussianAvatars [69].

Other changes. We attach the Gaussians to the triangles of the re-meshed FLAME model. Each Gaussian contains

a scale s , local position μ , local rotation r , spherical harmonics coefficients h , opacity α and parent triangle i . We initialize the avatar with $100K$ Gaussians, where the number of Gaussians for each triangle is proportional to the area of the triangle. Also, we set each Gaussian’s initial scale to be inversely proportional to the number of Gaussians per triangle, which we find to reduce rendering artifacts.

D. Datasets

We train the MMDM using the monocular video dataset VFHQ [92], and the multi-view datasets Nersemble [50], MEAD [88] and Ava-256 [63]. For MEAD, we use the sequences with neutral emotions. For Ava-256, we randomly select 20 sequences with 16 camera views for each subject. We jointly estimate 3DMM parameters, camera extrinsics and intrinsics using a multi-view face tracker [83]. For Nersemble and Ava-256, we use the available camera calibration. We remove frames where less than 95% of the head is visible. For VFHQ, we detect and remove videos with scene changes by checking the acceleration of the keypoints detected using the face tracker. Also, we use Mediapipe [107] to detect and remove frames containing hands, and we use the face tracker to detect and remove frames containing multiple faces. We estimate the gaze direction using a gaze estimation model [1] and convert it to the eye rotation of the FLAME model. In multi-view sequences, we use the most forward-facing view to estimate eye gaze. During training, we randomly select R reference images and G target images from all views and frames within a sequence with equal probability.

E. Evaluation

In this section, we provide details on our implementation, additional evaluation metrics, and additional ablations.

E.1. Implementation

We use the same predicted FLAME parameters to evaluate our method and our implementations of FlashAvatar [91] and GaussianAvatars [69]. The FLAME expression and identity shape parameters are extracted for each set of reference images [83]. Then, we fit expression parameters to the target frames while preserving the identity parameters.

All metrics for self-reenactment are measured after center-cropping to the head region, resizing to 512×512 resolution, and removing the background using masks included in the Nersemble dataset.

E.2. Additional Metrics

We provide results with the structural similarity metric SSIM, and following previous work [19, 51], we evaluate the average expression distance (AED) and average pose distance (APD) predicted using DECA [28] for both self

and cross-reenactment. For cross-reenactment, only the jaw pose distance is used. We measure the average keypoint distance (AKD) using facial landmarks predicted from a keypoint detector [13]. We report these additional metrics for self-reenactment with different numbers of reference images in Tab. S1, and for cross-reenactment in Tab. S2. The metrics show that our approach outperforms the baselines for the self-reenactment task. For cross-reenactment, our method and the baselines all have similar quantitative scores, but our approach shows clear improvements, as demonstrated in the user study and qualitative results.

E.3. User Study

For each video pair, we ask each participant questions to assess their preference in the following criteria using the following prompts.

- **Visual Quality (VQ):** Evaluate the clarity and visual appeal of each video. Your assessment should focus on the face and head region and ignore the neck and upper body.
- **Expression Transfer (EQ):** Determine which generated avatar’s facial expressions better match the driving video.
- **3D Structure (3DS):** Assess how well the 3D structure of the head is preserved across different viewing angles and expressions.
- **Temporal Consistency (TC):** Examine how smoothly and naturally the avatar maintains consistent appearance, expression, and movement across consecutive video frames.
- **Overall Preference (OP):** State your overall preference between the two videos. This is your subjective appraisal of which avatar, in your view, performs better.

The video pairs are presented in a random order, and each participant is asked to select either the left or right video for each criterion. We collect a total number of 4800 responses from 24 participants and conduct χ^2 -tests to evaluate statistical significance at the $p < 0.05$ level.

E.4. Additional Results

We provide additional self-reenactment and cross-reenactment results in Figs. S5 and S6. For self-reenactment, we directly compare our method to baselines with one, ten, or 100 reference images. As the number of reference images increases, our approach (both MMDM-only and CAP4D) improve in quality. With 100 reference images, we recover fine details in the hair and blemishes on the face. Our approach better preserves the identity and exhibits higher visual fidelity compared to baselines in the case of one reference image. We improve photorealism compared to baselines using ten or 100 reference images. The cross-reenactment results show trends similar to those in the main text. Compared to baselines, CAP4D better preserves the identity and fine details of the hair, face, and attire.

single reference image				
Method	SSIM \uparrow	AED \downarrow	APD \downarrow	AKD \downarrow
Voodoo3D [86]	0.658	1.463	0.085	10.52
GAGAvatar [19]	0.718	1.076	0.069	13.01
Real3D [100]	0.667	1.561	0.118	15.91
Portrait4D-v2 [23]	0.651	1.291	0.121	19.97
MMDM only	0.730	0.707	0.041	5.82
CAP4D	0.748	0.782	0.041	5.68

10 reference images				
Method	SSIM \uparrow	AED \downarrow	APD \downarrow	AKD \downarrow
DiffusionRig [24]	0.624	0.930	0.084	17.8
FlashAvatar [91]	0.580	1.243	0.124	20.8
GaussianAvatars [69]	0.628	1.413	0.237	21.5
no MMDM	0.590	1.064	0.093	10.6
MMDM only	0.753	0.542	0.033	5.09
CAP4D	0.748	0.782	0.041	5.68

100 reference images				
Method	SSIM \uparrow	AED \downarrow	APD \downarrow	AKD \downarrow
DiffusionRig [24]	0.617	0.975	0.085	18.6
FlashAvatar [91]	0.741	0.689	0.042	6.16
GaussianAvatars [69]	0.713	0.737	0.062	9.01
no MMDM	0.675	0.653	0.058	7.88
MMDM only	0.754	0.535	0.032	5.07
CAP4D	0.763	0.634	0.035	5.21

Table S1. **Additional single-image (top) and multi-image (middle, bottom) self-reenactment metrics.** Our method consistently outperforms baselines in terms of expression accuracy (AED), photometric quality (SSIM) and alignment accuracy (AKD).

Method	AED \downarrow	APD \downarrow
Voodoo3D [86]	2.428	0.082
GAGAvatar [19]	2.137	0.079
Real3D [100]	2.581	0.104
Portrait4D-v2 [23]	2.084	0.071
Ours	2.138	0.089

Table S2. **Additional cross-reenactment metrics.** We report additional metrics for our cross-reenactment evaluation.

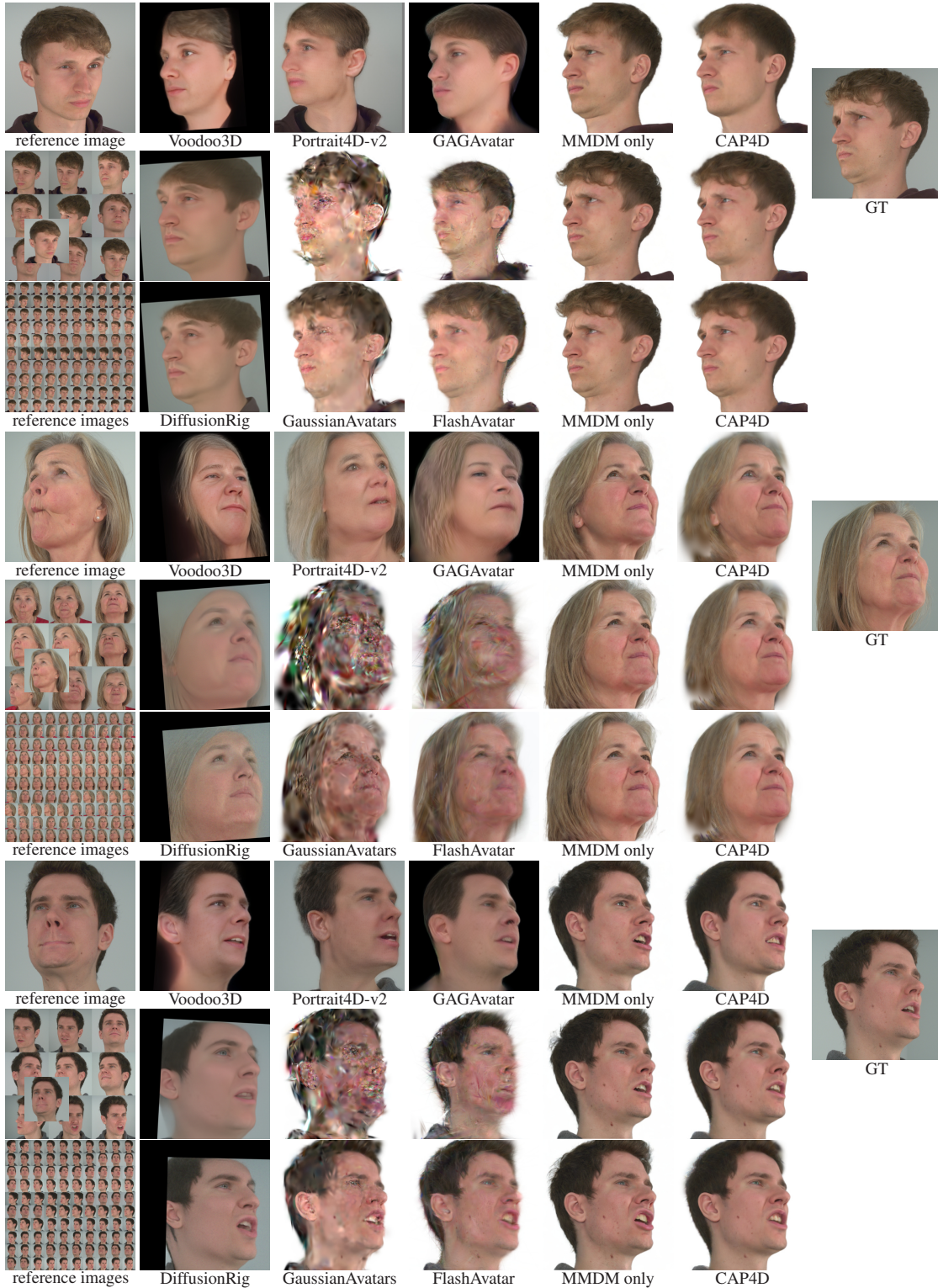


Figure S5. **Self-reenactment results.** We show more qualitative results for our self-reenactment evaluation with varying numbers of reference frames. Both our MMDM and final 4D avatar can leverage additional reference images to produce details that are not visible in the first reference image (hair, top three rows: birthmarks, last three rows). Our results are significantly better compared to previous methods, especially when the view direction differs greatly from the reference image.

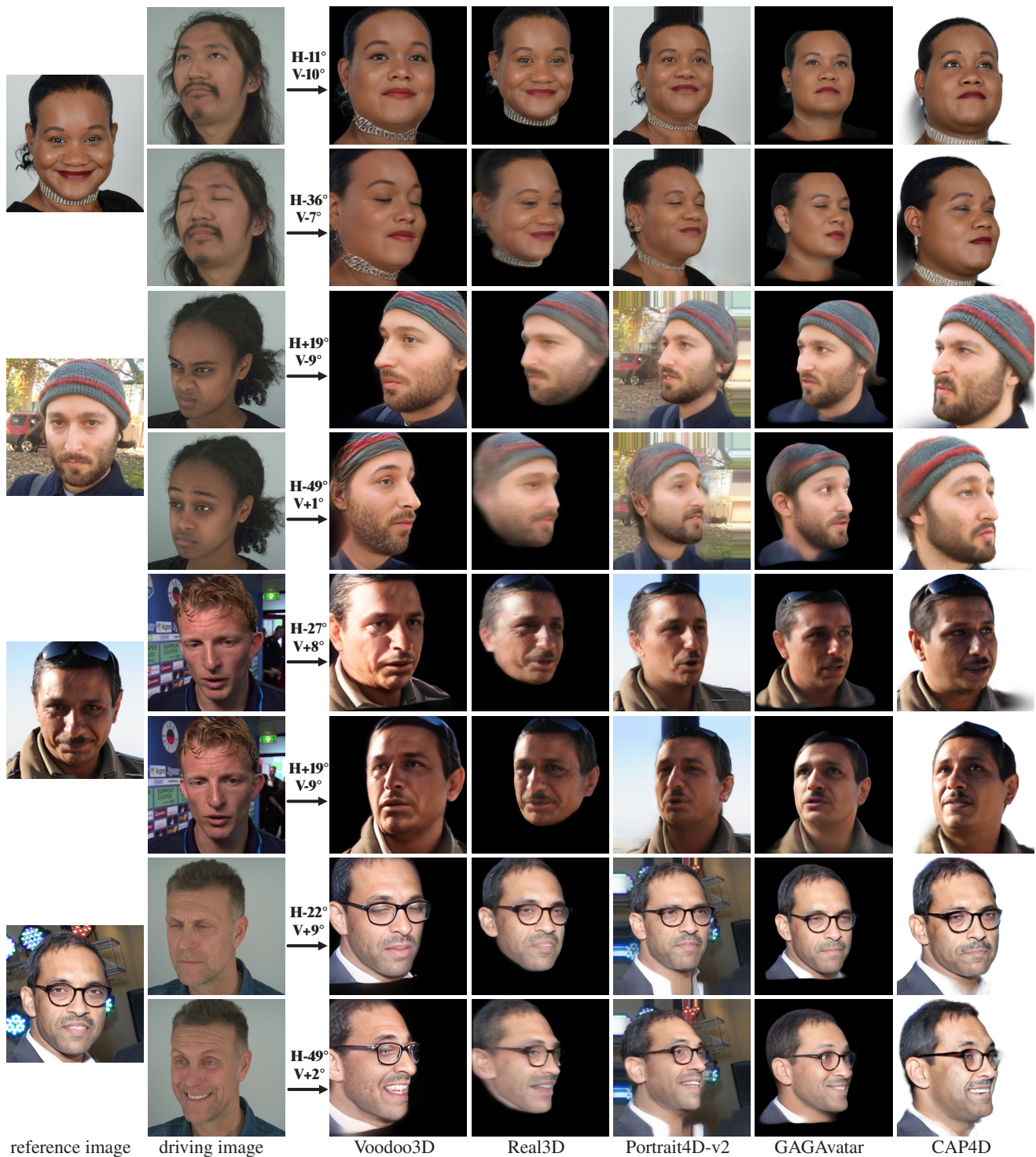


Figure S6. **Cross-reenactment results.** We show additional qualitative results of our cross-reenactment evaluation. We show generated frames under different driving expressions and viewing angles. Our method consistently produces 4D avatars of higher visual quality and 3D consistency even across challenging view deviations. Our avatar can also model realistic view-dependent lighting changes (row 5 and 6). Best viewed zoomed in.



Figure S7. **Ablations on stochastic I/O sampling.** We generate 14 images from a single reference image (left). Parts of the body do not appear in the reference image (shirt) and are thus ambiguous. When we generate these images without stochastic I/O sampling, two batches of seven images are generated separately (i.e., the third and last rows). This results in visible inconsistencies, such as a changing shirt pattern (red boxes). Stochastic sampling (first and second row) generates these images with information shared across all frames, resulting in a consistent shirt appearance.

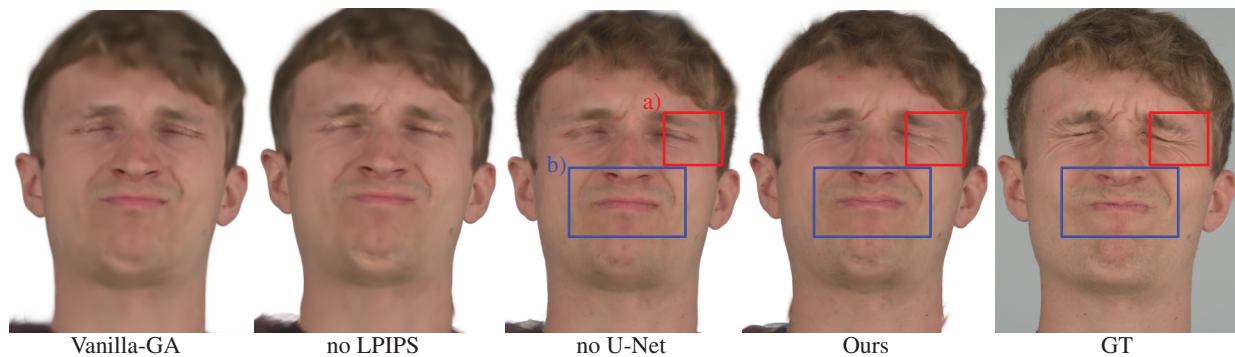


Figure S8. **Ablations on 4D avatar.** We show qualitative results with ablations of our 4D avatar for self-reenactment, using 10 reference images and images generated using the MMDM. From the left: The original implementation of GaussianAvatars without modifications (Vanilla-GA), our model without LPIPS loss (no LPIPS), our model without the U-Net correcting deformations (no U-Net), our final version (Ours), and the ground truth (GT). Without LPIPS, the avatar appears significantly more blurry. With the U-Net deformations, dynamic details such as wrinkles are depicted more accurately (wrinkles in (a)), and expressions are depicted overall more accurately (lips and nasio-labial fold in (b)).

Category	Ablation	PSNR \uparrow	LPIPS \downarrow	CSIM \uparrow	JOD \uparrow
sampling (single ref.)	w/o stochastic	21.60	0.325	0.625	5.31
	Ours	21.82	0.317	0.632	5.40
4D rep.	w/o stochastic	21.50	0.320	0.624	5.60
	$G = 420$	21.37	0.328	0.620	5.48
	Ours ($G = 840$)	21.69	0.311	0.633	5.67
	$G = 1260$	21.71	0.313	0.632	5.69

Table S3. **Additional ablations.** We assess the impact of our stochastic I/O conditioning with a single reference image. Also, we show the impact of stochastic I/O conditioning, and the number of generated images on the 4D reconstruction.

E.5. Additional Ablation Study

Stochastic I/O sampling. We conduct experiments with and without the stochastic I/O sampling on the self-reenactment task with a single reference image, and report the results in Tab. S3. With only a single reference image, stochastic sampling improves image quality (PSNR and LPIPS) and consistency between frames (JOD).

In Fig. S7, we illustrate the improved consistency by generating a toy set of 14 images. Inconsistencies such as changing shirt patterns appear without stochastic sampling, whereas using stochastic sampling improves overall consistency.

4D avatar. We conduct additional ablations on the ten-reference-image self-reenactment task (see Fig. S8 and Tab. S3); we show the impact of our improvements to the GaussianAvatars representation [69] and the impact of stochastic I/O sampling and varying the number of generated images on the quality of the 4D avatar. Qualitatively, adding the LPIPS loss and expression-dependent deformations predicted by the U-Net improves the ability to reconstruct wrinkles and expression-dependent details (Fig. S8).

The number of generated images also affects the quality of the avatar. Specifically, we evaluate generating $G = 420$, 840, or 1260 images and reconstructing the avatar. When generating fewer images, we observe worse reconstruction (LPIPS); adding additional images beyond $G = 840$ does not significantly improve the results, but requires additional compute. We also find that stochastic sampling improves the 4D avatar in terms of PSNR, LPIPS, CSIM, and JOD.

More reference images. Finally, we conduct an additional experiment with 400 reference images, which we evaluate the same way as previous experiments on the self-reenactment task. Evaluations (plotted in Fig. S9) show that while the performance of our MMDM plateaus, the final 4D avatar can leverage and scale with hundreds of reference images. This is likely because the 4D avatar can improve its reconstruction from the reference images through the direct optimization procedure.

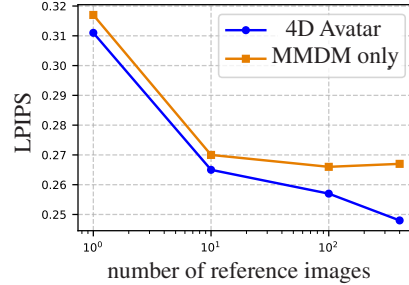


Figure S9. **Analysis of Reference Quantity.** We observe that with hundreds of reference images, the performance of the MMDM plateaus, while our 4D avatar continues scaling with the input quantity. This shows that the 4D avatar can seamlessly benefit from both generated and reference images.

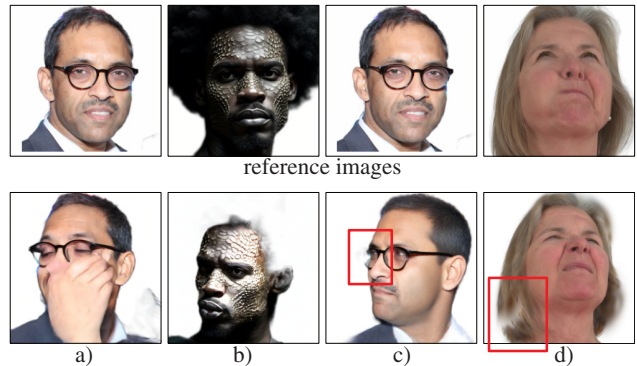


Figure S10. **Failure Cases.** (a) Our training dataset contains some images that were not properly filtered out using our automated pipeline, and so the MMDM sometimes generates images where the face is occluded (e.g., by a hand). (b) Some training images contain a faulty background segmentation, occasionally leading to artifacts in the MMDM output. (c) Our 4D avatar can fail in areas not modeled by the FLAME topology, such as glasses and (d) long hair.

E.6. Failure Cases

We show failure cases for the MMDM and the 4D avatar in Fig. S10. Specifically, we find that some generated images reflect imperfections in our training dataset, such as images where a hand occludes the face, or images where there are artifacts due to imperfect background segmentation. Also, the 4D avatar cannot model certain regions perfectly, such as hair or glasses, since these are not modeled in the FLAME topology.